The Thesis committee for Ethan Stewart Rapp

Certifies that this is the approved version of the following thesis:

Brushless DC Motor Modeling and Optimal Control: A Cardiovascular Application

APPROVED BY

SUPERVISING COMMITTEE:

Raul G. Longoria, Supervisor

Dongmei "Maggie" Chen

Brushless DC Motor Modeling and Optimal Control: A Cardiovascular Application

by

Ethan Stewart Rapp, B.S.

Thesis

Presented to the Faculty of the Graduate School

of the University of Texas at Austin

in Partial Fulfillment

of the Requirements

for the Degree of

Master of Science in Engineering

The University of Texas at Austin

August 2016

Brushless DC Motor Modeling and Optimal Control: A Cardiovascular Application

by

Ethan Stewart Rapp, MSE

The University of Texas at Austin, 2016

SUPERVISOR: Raul G. Longoria

The increasing use of Ventricular Assist Devices (VADs) in patients with weak or failing hearts has driven a need for more thorough analysis of VAD design, control methods, and cardiovascular dynamic effects. In recent years, studies have shown the potential of applying formal optimization methods to VAD actuation in order to reduce power consumption or improve pump output. This thesis continues the use of formal optimization methods as well as digital analysis using the brushless DC (BLDC) motors within the TORVAD^{TM}, designed by Windmill Cardiovascular Systems, Inc. (WCS), as a basis.

To begin the optimization, a parameterized model of the BLDC motor system has been developed and combined with a lumped parameter model of the cardiovascular system. The combined system is then digitally analyzed under varying rates of TORVAD^{TM} motor controller frequencies to determine the minimum frequency at which the system will remain stable and minimize detrimental physiological effects.

Formal optimization methods are then introduced and implemented on the combined motor and cardiovascular system model. The output of the optimization is a reference trajectory that minimizes average motor power consumption. This trajectory, along with the results from the digital analysis, provides a more robust examination on the combined motor and cardiovascular system.

Contents

List of Tables

List of Figures

1. Introduction

Ventricular Assist Devices (VADs) are implantable pumps used to improve blood circulation in patients with weak or failing hearts by drawing blood from the ventricle and pumping back into the corresponding aorta. These devices were originally intended as a bridge to transplant measure for patients waiting for a new heart, but have increased their potential in recent years with bridge to recovery and bridge to destination (or destination therapy) considerations in both pediatric and adult conditions [12, 13, 14].

As their applications increase, so does the emphasis on robust design and performance of both pulsatile and continuous flow VADs. But these emphases can come at a cost, such as increased VAD size or the fusion of aortic leaflets[1]. The tradeoff between beneficial and detrimental design features drives the need for VAD optimization. Most notably, optimization to improve design for hemodynamic performance, size reduction, power consumption, and physiological response while assessing the merits of both continuous flow and pulsatile VADs.

Through the combination of cardiovascular system and ventricular assist device models, studies have been performed that delve into the dynamic coupling of the two systems in order to determine the optimal performance range of the VAD itself. Namely, how VAD modes of actuation affect the cardiovascular system in terms of systemic hemodynamics[2].

In the case of Amacher *et al.*, optimal pulsatility of a turbo dynamic VAD[3] at the cost of stroke work was evaluated in order to facilitate better hemodynamic performance over time compared to the original continuous flow pumping profile [1]. The work of Tavoularis *et al.* pushes the optimal control problem a step further by fo-

[1]Aortic leaflet fusion occurs when there is not enough blood flowing through the aortic valve to force it to open[21].

[2]Systemic hemodynamics refers to the level of blood pressure (mean arterial pressure) and flow rate at the output of the left heart, which reflect health issues such as thrombosis and hemolysis.

[3]Turbo Dynamic VAD (tVAD): A continuous flow VAD with speed adjustment capabilities

cusing on the shear stresses and flow gradient of the output blood flow, which more specifically relate to how hemodynamic issues arise [3].

In practice, the work of Klute *et al.* have successfully implemented an optimal control scheme on an EVAD (electric-VAD) that improved the efficiency of the VAD compared to the original adaptive feed-forward control scheme. However, the hemodynamics of the cardiovascular system were not studied in this paper, meaning only the EVAD power consumption was taken into account during the optimization [2].

A last example of optimal control analysis in VAD systems comes from Yoshizawa *et al.* where the optimal point of actuation was evaluated with respect to the cardiovascular system in order to avoid hemodynamic issues and minimize pump energy. This paper also concluded that the optimal control scheme was preferable to the original Proportional-Integral (PI) control scheme, but improvements could be made such that the system would converge faster to an optimal operating point [4].

Despite the many analyses of control methods for VADs, there have been few studies in the area of optimization methods. The rise in optimization considerations could potentially be due to the increasing capabilities of computer models to more accurately represent the cardiovascular system, both by itself and with an incorporated VAD model. Also, a great scope of experimental testing data in patients or animals is widely available and can be used to better tune both software models and physical systems, such as hardware-in-the-loop simulations.

This thesis explores the use of formal optimization methods towards the actuation of the brushless DC (BLDC) motors found within the Toroidal Ventricular Assist Device (TORVAD$^{\text{TM}}$) created by Windmill Cardiovascular Systems, Inc. (WCS). Previously, hemodynamic performance considerations for the TORVAD$^{\text{TM}}$ have been made through the work of Gohean *et al.* in terms of the selection of ejection timing during the cardiac cycle, [18], and comparisons between TORVAD$^{\text{TM}}$ performance and that of continuous flow pumps [19, 20]. Optimal piston stroke trajectory was also addressed, but without formal optimal control methods. Instead, successive simulations allowed for the 'optimal' performance to be determined by brute force. By implementing formal optimization methods, a more robust analysis of optimal performance can be achieved towards the goal of improving patient hemodynamic trends and VAD dependency.

The TORVAD$^{\text{TM}}$ is a synchronous, positive-displacement VAD that houses two independently controlled pistons within a toroidal pumping chamber. Rare earth

magnets are sealed within each piston and interact with magnetic, C-shaped rotational arms that are housed on the outside of the toroidal chamber. The rotational arms are directly connected to position controlled BLDC motors. During actuation of the TORVAD^{TM}, one piston is held stationary between the input and output cannulae while the other piston is driven through the toroidal chamber, providing blood flow to the left aorta. Once the driving piston reaches the output cannula, the two pistons rotate in unison and swap initial pumping positions - the stationary piston rotates to the initial drive position and the drive piston rotates to the stationary position between both cannulae. A figure of TORVAD^{TM} actuation and chamber cross-section are provided in Figure 1.1.

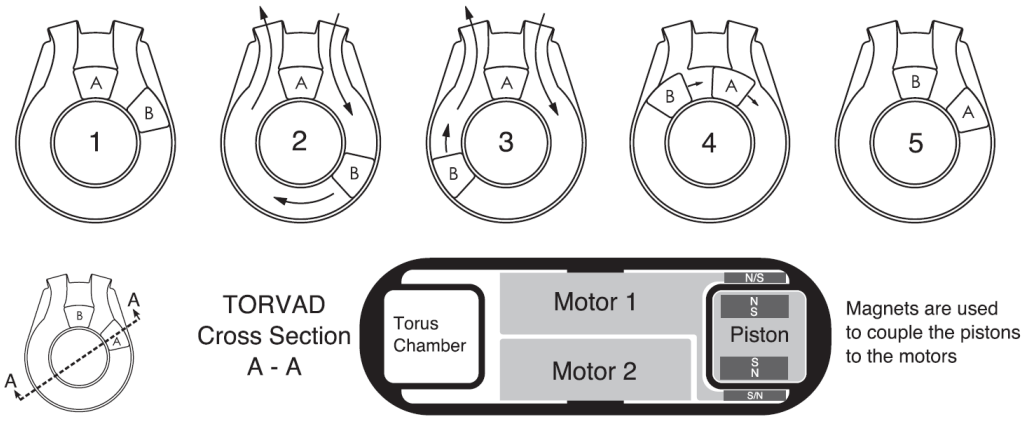

Figure 1.1: WCS TORVAD^{TM} actuation method and cross-section.

The actuation methods of the toroidal pump add difficulty during the optimization process. Rather than optimizing actuation around a single operating point, as was done in [2, 4], an optimal operating trajectory must be found that optimizes motor performance throughout the entire timespan of motor actuation.

Figure 1.2 provides another representation of the TORVAD^{TM} system with the BLDC motor controlled pistons shown within the toroidal chamber of the pump connected to the left heart. Each has the ability to rotate $\pm$ 360°and must be continually monitored to prevent collisions and detrimental physiological effects.

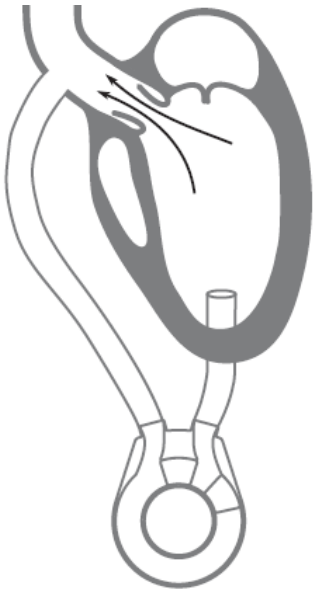

Figure 1.2: WCS TORVAD^{TM} providing blood flow from the left ventricle (right cannula connection) into the left aorta (left cannula connection).

In order to apply optimization algorithms to the TORVAD^{TM}, first a parameterized model of the BLDC motor system was developed in Chapter 2. Second, a discrete time (digital) control analysis was performed in Chapter 3 on the BLDC motor system model integrated with a simplified cardiovascular system (CVS) model. This analysis allowed for the determination of a suitable sampling time for motor control. And third, optimal control techniques were applied in Chapter 4 in order to determine a "Power-Saving" mode of actuation that minimized the amount of power consumed in a single stroke of the internal piston. In other words, a stroke trajectory for the toroidal piston was found that minimizes instantaneous power draw at each moment in time while still meeting all physiological and time constraints. This optimal trajectory is used as a reference in the TORVAD^{TM} controller during actuation to drive the piston to its desired position along the optimal path.

2. Parameterized Brushless DC (BLDC) Motor Model

Brushless DC (BLDC) motors require a DC power input that is commutated[1] into a three-phase AC signal using a specified commutation scheme. The three-phase AC signal is sent through the BLDC motor stator windings to induce a magnetic flux that attracts or repulses the permanent magnets within the rotor (for the case of a permanent magnet rotor), forcing rotor rotation. In this chapter, a parameterized, nonlinear state space model of each BLDC motor is established in Section 2.1, a discussion of TORVAD$^{\text{TM}}$ motor commutation and control is provided in Section 2.2, typical motor performance is shown in Section 2.3, and Section 2.4 provides a brief summary.

2.1 Model States

The nonlinear, time-invariant relationship between the three-phase flux linkages and mechanical system is defined below following the work of Krause *et al.* [5].

$X \in \mathbb{R}^5$: The state matrix of dynamic states in the BLDC motor system

$$X = \begin{bmatrix} \lambda_{as} & \lambda_{bs} & \lambda_{cs} & \omega_r & \theta_r \end{bmatrix}^T$$

evaluated over the time interval

$$t \in [t_0, t_f].$$

The motor variables are provided below.

- λ_{abcs}: The magnetic flux of the A, B, or C phase of the commutated power

[1] Commutation is the process of using a three-phase power bridge, a rotor-position encoder, and logic-gate array to switch the DC input signal into a three-phase AC signal based on rotor position [6].

input $[Vs]$

- ω_r: The electrical angular velocity of the rotor $[\frac{rad}{s}]$
- θ_r: The electrical angular position of the rotor $[rad]$

The control input to the BLDC motor system is the voltage duty cycle, which translates into a three-phase voltage input after commutation.

$U \in \mathbb{R}^3$: Control input to BLDC motor system, where the corresponding voltages for each AC phase are,

$$U(t) = V_{abcs} = \begin{bmatrix} V_{as}(\theta_r) & V_{bs}(\theta_r) & V_{cs}(\theta_r) \end{bmatrix}^T,$$

where V_{as} represents the voltage for AC phase A, V_{bs} for AC phase B, and V_{cs} for AC phase C.

The nonlinear dynamic equations of these states are provided in the equations below, starting with the magnetic flux linkages of each AC phase, λ_{abcs}.

$$\dot{\lambda}_{abcs} = -R_S\, I_{abcs} + V_{abcs} \tag{2.1.1a}$$

which can be written in matrix form as,

$$\dot{\lambda}_{abcs} = \frac{d}{dt}\begin{bmatrix} \lambda_{as} \\ \lambda_{bs} \\ \lambda_{cs} \end{bmatrix} = -\begin{bmatrix} R_S & 0 & 0 \\ 0 & R_S & 0 \\ 0 & 0 & R_S \end{bmatrix}\begin{bmatrix} I_{as} \\ I_{bs} \\ I_{cs} \end{bmatrix} + \begin{bmatrix} V_{as} \\ V_{bs} \\ V_{cs} \end{bmatrix}, \tag{2.1.1b}$$

where R_S represents the stator resistance and I represents the current for each AC phase. For example, I_{as} is the current in AC phase A, whereas I_{bs} represents the current in AC phase B. Again, V represents the duty cycle voltage input for each AC phase.

The phase currents, I_{abcs}, are related to the state variables according to the equation,

$$I_{abcs} = L_s^{-1}(\lambda_{abcs} - \underline{\lambda'_m}), \tag{2.1.1c}$$

where the stator inductance matrix, L_s, is defined as,

$$L_s = \begin{bmatrix} L_{ls} + L_{ms} & -\frac{1}{2}L_{ms} & -\frac{1}{2}L_{ms} \\ -\frac{1}{2}L_{ms} & L_{ls} + L_{ms} & -\frac{1}{2}L_{ms} \\ -\frac{1}{2}L_{ms} & -\frac{1}{2}L_{ms} & L_{ls} + L_{ms} \end{bmatrix}, \tag{2.1.1d}$$

where inductance terms L_{ls} and L_{ms} are the leakage inductance of a single motor phase and the magnetizing inductance, or mutual inductance between phases, respectively.

The flux linkage matrix due to the permanent magnet, $\underline{\lambda_m^{'}}$, is expanded as,

$$\underline{\lambda_m^{'}} = \lambda_m^{'} \begin{bmatrix} sin(\theta_r) \\ sin(\theta_r - \frac{2\pi}{3}) \\ sin(\theta_r + \frac{2\pi}{3}) \end{bmatrix}, \tag{2.1.1e}$$

where $\lambda_m^{'}$ is the amplitude of the permanent magnet flux linkages per each stator phase winding. This equation is based on the assumption that the voltages induced in the stator windings by the permanent magnet are constant amplitude sinusoidal voltages.

The dynamic equation for the state of electrical angular velocity, ω_r, can be expressed as,

$$\dot{\omega}_r = \Big(\frac{P}{2}\Big)\frac{\tau_e - \tau_L - (\frac{P}{2})B\omega_r}{J_{total}}, \tag{2.1.2a}$$

where τ_e is the electromagnetic drive torque (the torque from the back electromotive force), τ_L is the torque from any load acting on the rotor, J_{total} is the total rotational moment of inertia of the rotor and the piston connected to the rotor, P is the number of stator poles, and B is the linear damping coefficient.

The electromagnetic drive torque is solved using,

$$\tau_e = \Big(\frac{P}{2}\Big)\lambda_m^{'}\Big[\Big(I_{as} - \frac{1}{2}I_{bs} - \frac{1}{2}I_{cs}\Big)cos(\theta_r) + \frac{\sqrt{3}}{2}(I_{bs} - I_{cs})sin(\theta_r)\Big], \tag{2.1.2b}$$

which is derived by differentiating the coenergy of the magnetic field with respect to

electrical angle, θ_r. The last dynamic equation is for the electrical angular position, θ_r, which is simply the integral of the electrical angular velocity with respect to time,

$$\dot{\theta}_r = \omega_r. \tag{2.1.3}$$

Note that this is the electric angle (and electrical angular velocity for ω_r). The relationship between electrical angle, θ_r, and stroke angle, θ_m, is based on the number of stator poles within the motor,

$$\theta_m = \Big(\frac{2}{P}\Big)\theta_r. \tag{2.1.4}$$

This relationship holds for electrical angular velocity and stroke velocity as well, which can be derived through taking the time derivative of each side of the equation. Since the number of poles within the stator do not change with time, the relationship is a constant factor of $\frac{2}{P}$.

Using the equations derived from Krause *et al.*, an equivalent bond graph representation of a single BLDC motor is presented in Figure 2.1. This bond graph will be integrated in later sections with cardiovascular system and test apparatus models.

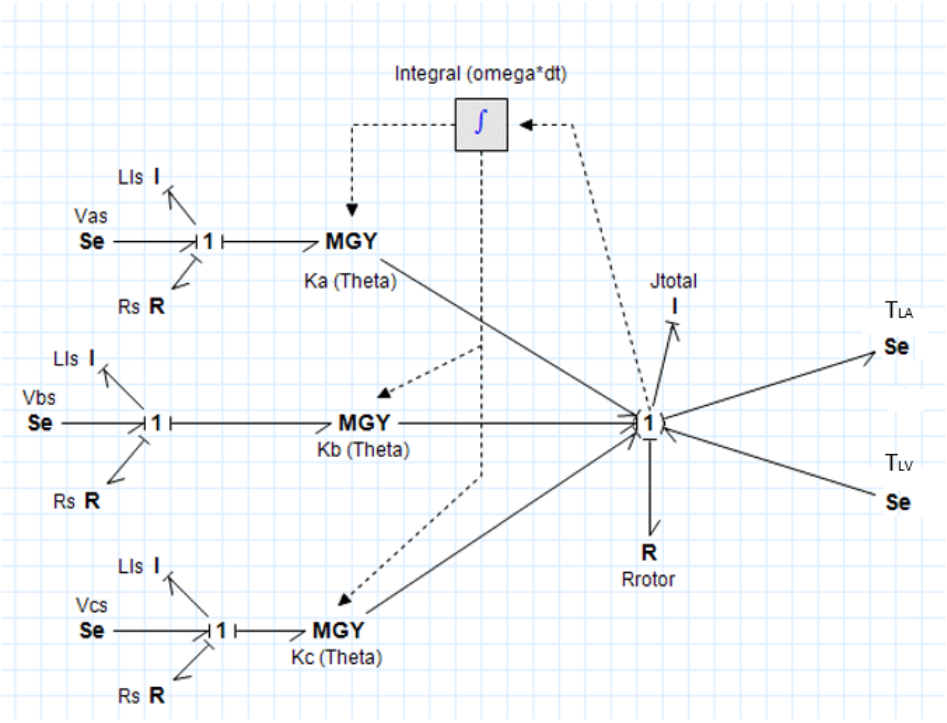

Figure 2.1: TORVAD^{TM} BLDC motor bond graph.

The BLDC motor bond graph is shown with three input voltages (equivalent to AC voltages after the DC to AC commutation) connected to gyrators that use the electrical angular position as the modulus. Each modulated gyrator transfers power to the mechanical piston which counteracts the equivalent torques caused by the left ventricle and aortic pressures within the cardiovascular system. The modulus functions, or motor constants, for each phase are provided in the Appendix section of this thesis.

The states within the bond graph are represented by the energy storing, inertial components which represent inductance in the electrical circuit and angular momentum in the mechanical system. Each inertial component is shown with independent causality, meaning each of these states are independent from one another in the simulation. The mutual inductance of each AC phase acting upon one another is omitted in the bond graph for visual clarity.

2.2 Commutation Scheme and Control

Permanent-magnet, synchronous motors involve the use of a three-phase stator, which can be wound in multiple ways. Common winding configurations include the trapezoidal distribution, classified as BLDC motors, and sinusoidal distribution, classified as sine-wave-wound, permanent-magnet, synchronous motors. Since the input to the BLDC motors is not three-phase, the input signal must be controlled using a three-phase power bridge, a rotor-position-measurement system, and commutation logic with PWM to produce a three-phase input [6]. Figure 2.2 depicts a common circuit for DC to three-phase AC commutation.

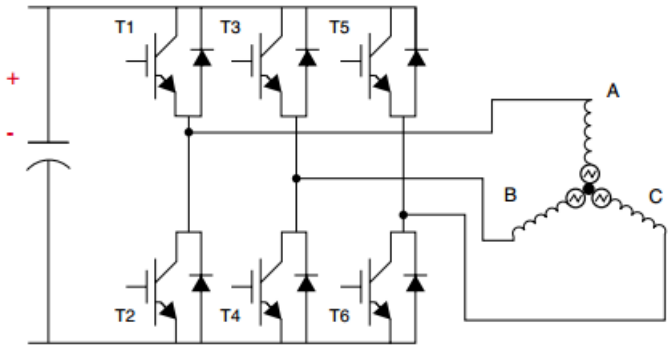

Figure 2.2: TORVAD^{TM} BLDC motor wye commutation circuit [22].

2.2.1 Commutation Methods

Two commutation methods were explored during this research. The first was a six-step commutation method that involves switching the three phase voltages on or off based on rotor position. The implementation of this method is well established, but there are certain performance criteria considerations that need to be made, such as implementing a delay for rise time and evaluating the cogging torque.

A figure of typical current output using a six-step commutation scheme on a BLDC motor is provided in Figure 2.3 below.

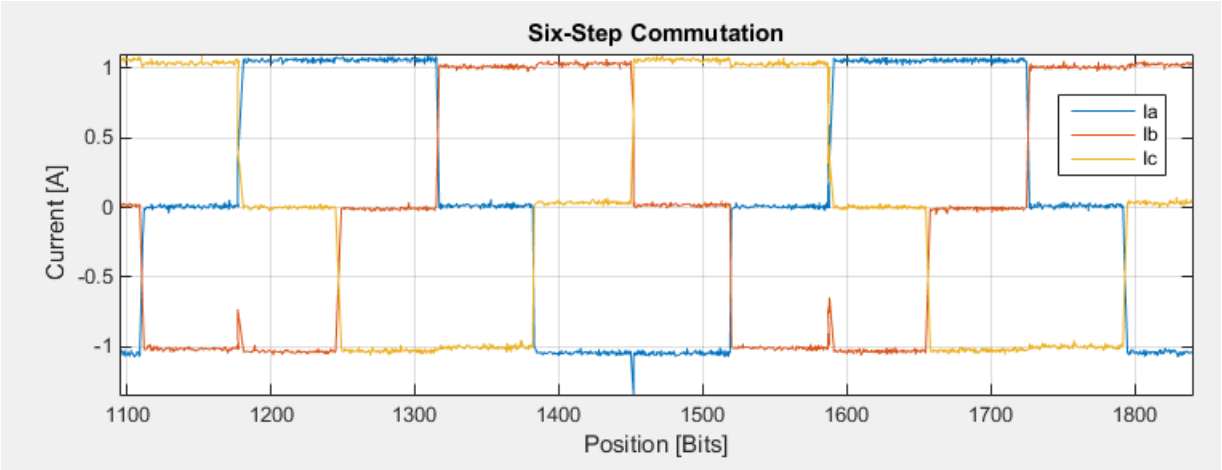

Figure 2.3: BLDC motor phase currents for six-step commutation method.

The second commutation method explored was sinusoidal commutation. In this method, the amplitude of each phase voltage is adjusted slightly, again based on rotor position, in order to simulate a three-phase sinusoidal input. This method eliminates the need for a controller delay due to rise time, as well as lessens the magnitude of physical cogging torques.

A figure of current output using a sinusoidal commutation scheme on a BLDC motor is provided in Figure 2.4 below.

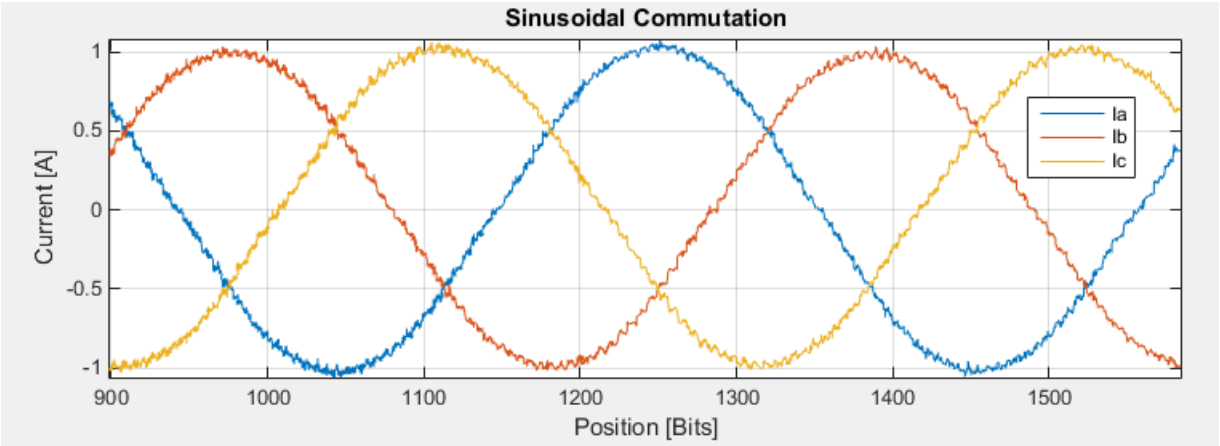

Figure 2.4: BLDC motor phase currents for sinusoidal commutation method.

Note: The x-axis units of position in Figures 2.3 and 2.4 are in [Bits]. These units correspond to a modulated electric angle position in the rotor position sensor employed by WCS through the relation of [0-4096 Bits] = [$0 - 2\pi$ radians].

2.2.2 Commutation Voltage Equations

The commutation voltage equations are based on six controllable switches, labeled T1-T6, within the three-phase bridge converter. When combined, these switches comprise the three-phase voltage input to the motor system [5]. In the case of the six-step commutation method, the switches are turned on or off suddenly and produce the three-phase currents shown in Figure 2.3. In the case of the sinusoidal commutation method, the switches adhere to a sinusoidal pattern of voltage amplitude and produce the three-phase currents shown in Figure 2.4.

In the six-step commutation method, the switches are controlled as shown in Figure 2.5 below.

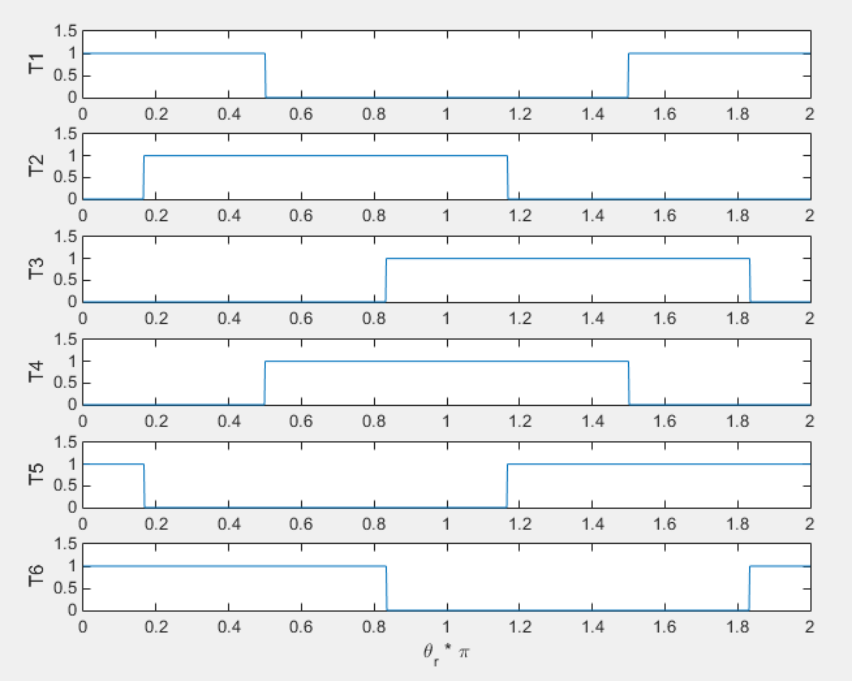

Figure 2.5: Six-step commutation switching pattern. A switch value of one (1) designates it as on, or powered, while a value of zero (0) designates the switch as off.

For the sinusoidal commutation scheme, the switch pattern in Figure 2.6 is produced.

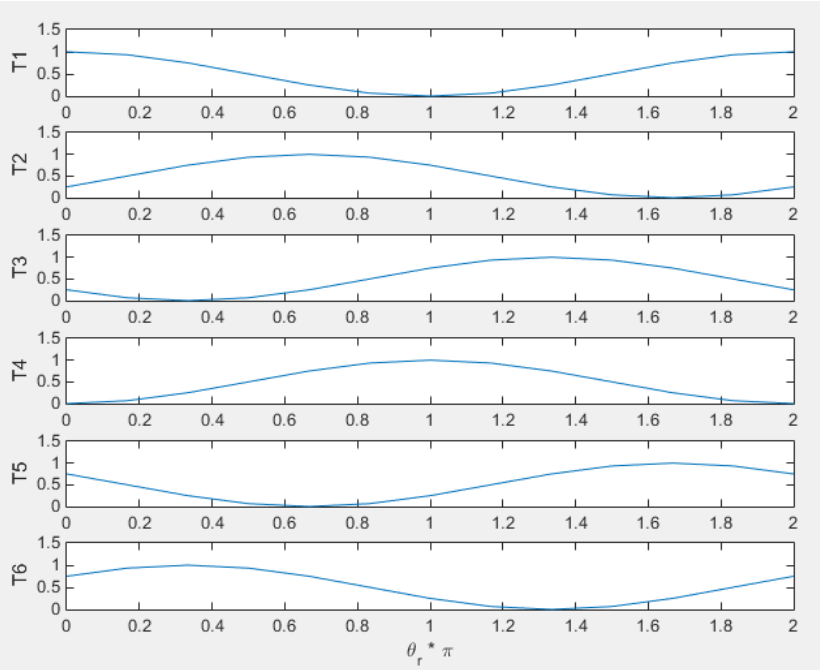

Figure 2.6: Sinusoidal commutation switching pattern.

The commutation scheme does not affect how the voltage of each phase is calculated. First, an interpolation is completed to solve for each switch value ($T1$-$T6$) based on the electric angle (modulated between 0 and 2π [rad]) at that moment in time. The switch values are then used to calculate phase voltages using,

$$V_{ap} = \frac{1}{2}(1 + T1 - T4)V_{in} \tag{2.2.1}$$

$$V_{bp} = \frac{1}{2}(1 + T2 - T5)V_{in} \tag{2.2.2}$$

$$V_{cp} = \frac{1}{2}(1 + T3 - T6)V_{in} \tag{2.2.3}$$

where V_{in} represents the total input voltage multiplied by the duty cycle.

To find the voltage between each winding of the stator, one phase is subtracted from another. As an example, the voltage between phases A and B is,

$$V_{ab} = V_{ap} - V_{bp}. \tag{2.2.4}$$

Lastly, the voltages supplied to each phase of the motor are,

$$V_{as} = \frac{2(V_{ap} - (V_{bp} + V_{cp}))}{3}, \tag{2.2.5}$$

$$V_{bs} = \frac{2(V_{bp} - (V_{ap} + V_{cp}))}{3}, \tag{2.2.6}$$

and

$$V_{cs} = \frac{2(V_{cp} - (V_{ap} + V_{bp}))}{3}. \tag{2.2.7}$$

2.2.3 Commutation Control

Rotor position dictates the commutation pattern of a BLDC motor. Typically, Hall-effect devices are used in order to obtain rotor position due to their low-cost, high reliability, and high operating frequencies (100+ KHz). In high-performance applications, however, resolvers and encoders can be used to ensure higher position resolution. These position sensors are used to relay position information to the commutation logic, which then tells the power bridge the appropriate magnitude of each phase voltage to output [6].

The TORVAD^{TM} motors (permanent-magnet, synchronous motors) have a trapezoidal winding distribution, but the controlled commutation pattern is sinusoidal. This decision was made to reduce audible noise and physical cogging torques that result when the six-step commutation method is used. As for the control aspect, the motors are equipped with encoders in order to gather high resolution position data for the commutation logic, while the motor controller runs at a frequency of 4800 Hz.

2.3 Typical Open-Loop Performance

Though the BLDC motor system voltage input is controlled through feedback position measurements, the commutated BLDC model established in this section will be referred to as the "open-loop" BLDC model for the remainder of this thesis. BLDC motor commutation is a minimum requirement for basic motor function and can be applied separately from any additional control scheme, hence the decision to denote the previous model as "open-loop."

A 96-point sinusoidal commutation scheme is used for the BLDC motors in the TORVAD^{TM}, therefore this will be the assumed commutation scheme for this section and for the remainder of this thesis.

Open-loop BLDC state performance is shown in the figure below for a constant input duty cycle to 30% (of the max voltage input of 14.9 [V]).

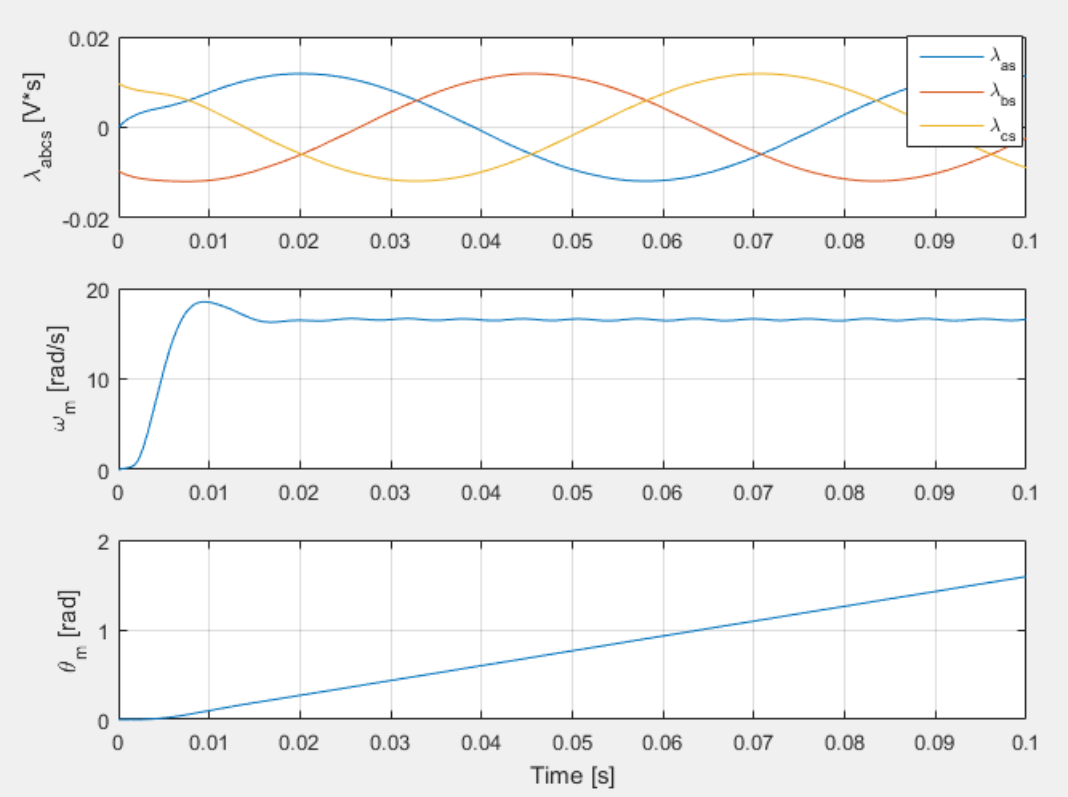

Figure 2.7: Open-loop state trajectories for input duty cycle of 30%.

Other notable performance variables include phase currents, I_{abcs}, phase voltages, V_{abcs}, and electromagnetic drive torque, τ_e, which are shown in the figure below.

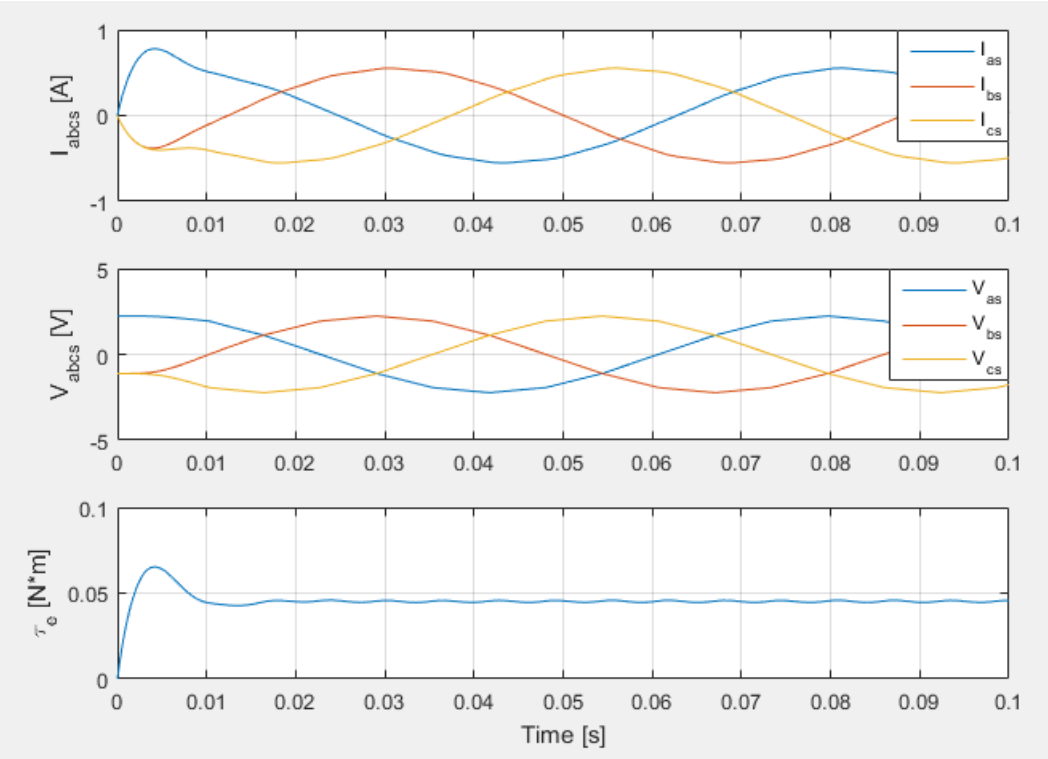

Figure 2.8: Open-loop system variable performance for input duty cycle of 30%.

Note the rippling effect seen in the electromagnetic drive torque, τ_e, and subsequently in the stroke velocity, ω_m. This is due to the sinusoidal commutation of the DC input and the position dependence of the flux linkage of the permanent magnet, $\lambda_m^{'}$.

2.4 BLDC Motor Model Summary

This chapter focused on building a parameterized model of a single BLDC motor within the WCS TORVAD^{TM}. This model is to be used as a basis for the following sections to build on in order to analyze and optimize the BLDC motor system performance. The commutation and open-loop performance were also discussed in order to provide a frame of reference for typical BLDC motor actuation.

3. Cardiovascular System Model Integration

As stated previously, the WCS TORVAD^{TM} is an implantable left-ventricular assist device for human patients with weak or failing hearts. When implanted, the heart pump draws blood from the left ventricle and pumps into the left aorta of the human heart. The rhythmic pressures of the left ventricle and left aorta apply dynamic forces on the front and rear faces of the BLDC rotor piston. These forces can be parameterized and added to Equation 2.1.2a contributing to the load torque variable, τ_L.

This chapter details the integration of the WCS CVS model in Section 3.1 into the working BLDC motor model in Section 3.2. This chapter also provides the first form of motor optimization in regard to power consumption in Section 3.3, which is the amount of power consumed by the motor controller and power electronics. Since the controller operates in discrete time, the combined motor and CVS model is digitally analyzed to determine how fast the motor controller must sample the system. A lower sampling rate decreases required input power, but can lead to instability or performance issues. Therefore, a balance must be struck in order to minimize power and keep motor and CVS trends within desired performance specifications. Section 3.4 provides a summary of digital analysis results.

3.1 CVS Model

The CVS model from WCS is based upon four volumetric states representing different areas of the cardiovascular system. These states are the volume of the left atria, V_{LA}, the volume of the left ventricle, V_{LV}, the volume of the systemic artery, V_{SA}, and the volume of the atrial tree, V_{AT}.

The dynamic equations of each volumetric state can be written as a difference in blood flows from varying parts of the cardiovascular system. Also, each volumetric

state is reliant on cardiac cycle timing[1]. The volume of the left atria is dependent on the flow difference between the right side of the CVS and the mitral valve, which is expressed as,

$$\dot{V}_{LA} = Q_{RS} - Q_{MI}, \tag{3.1.1}$$

where Q_{RS} is a function of the pressure and resistance of the right side of the CVS, as well as the left aorta pressure and elastance. Q_{MI} is a function of left aorta and left ventricle pressures and elastances, and mitral valve resistance.

The volume of the left ventricle is based on the flow difference between the mitral valve and the left atria (aortic valve), which is expressed as,

$$\dot{V}_{LV} = Q_{MI} - Q_{LA}, \tag{3.1.2}$$

where Q_{LA} is a function of the systemic artery volume and compliance, as well as the left ventricle pressure and elastance.

The volume of the systemic artery is dependent on the flow difference between the left atria (aortic valve) and the systemic artery, which is expressed as,

$$\dot{V}_{SA} = Q_{LA} - Q_{SA}, \tag{3.1.3}$$

where Q_{SA} is a function of the systemic artery pressure and resistance, and the atrial tree volume and compliance.

Lastly, the volume of the atrial tree is dependent on the flow difference between the systemic artery and the atrial tree, which is expressed as,

$$\dot{V}_{AT} = Q_{SA} - Q_{AT}, \tag{3.1.4}$$

where Q_{AT} is a function of the atrial tree pressure and resistance, as well as the venous system pressure.

Steady-state trends of the new volume states are shown below for a person with a heart-beat rate of 80 beats per minute [BPM].

[1]In this thesis, cardiac cycle timing refers to the timing of the heart beat in regard to the dynamic simulation time. Whether the heart chambers are filling or ejecting (i.e. heart chamber valves are open or closed) is based on the heart beats per minute and the simulation time iteration being evaluated.

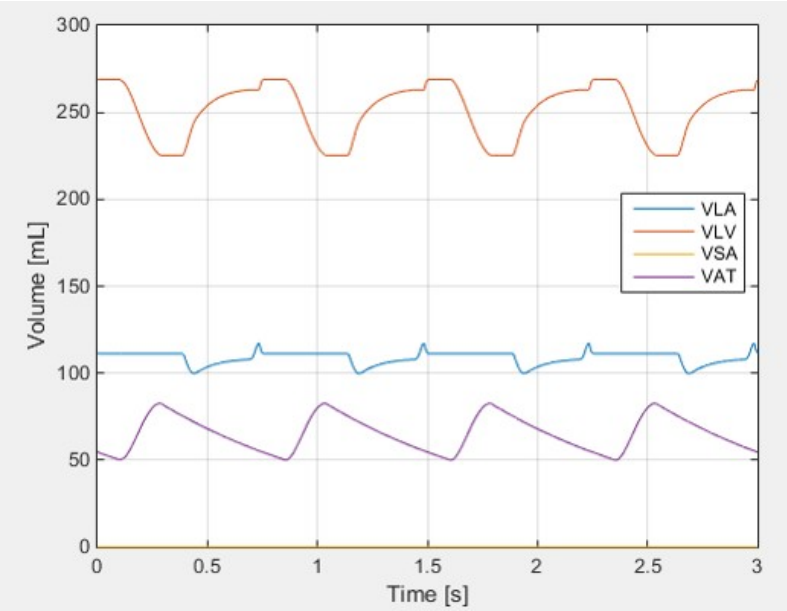

Figure 3.1: Steady-state volume trends for 80 BPM person.

The states that directly influence the WCS TORVAD^{TM} are the volume of the left ventricle (V_{LV}) and left atria (V_{LA}). These states relate to the dynamic pressures acting on each face of the motor piston as it actuates - the volume in the left ventricle applies pressure from the inlet cannula and the volume from the left atria applies pressure at the output cannula.

3.2 CVS and BLDC Model Integration

The original state matrix provided in Section 2.1 now incorporates the four new volume states established in Section 3.1

$X_{CVS} \in \mathbb{R}^9$: The state matrix of dynamic states in the combined BLDC motor and CVS system. The updated state vector is,

$$X_{CVS} = \begin{bmatrix} \lambda_{as} & \lambda_{bs} & \lambda_{cs} & \omega_e & \theta_e & V_{LA} & V_{LV} & V_{SA} & V_{AT} \end{bmatrix}^T,$$

over the time interval

$$t \in [t_0, t_f]$$

where V_{LA} is the volume of the left atria, V_{LV} is the volume of the left ventricle, V_{SA}

is the volume of the systemic artery, and V_{AT} is the volume of the atrial tree.

After incorporating the volumetric states, the only dynamic equation adjustment that needs to be made for the BLDC motor described in Section 2.1 is the definition of the load torque, τ_L, in Equation 2.1.2a. The new load torque becomes,

$$\tau_L = L_{eff} A_p (P_{LV} - P_{LA}), \tag{3.2.1}$$

where L_{eff} is the effective length of the rotational arm of the piston, A_p is the surface area of the piston face, P_{LV} is the pressure of the left ventricle, and P_{LA} is the pressure of the left atria.

The left ventricle and left atria dynamic volumetric states are updated as well due to the blood flow being pulled into the TORVAD$^{\text{TM}}$ from the left ventricle and being forced out into the left atria. The new dynamic equations become,

$$\dot{V}_{LV} = Q_{MI} - Q_{LA} - L_{eff} A_p \frac{2}{P} \omega_e, \tag{3.2.2}$$

and

$$\dot{V}_{LA} = Q_{RS} - Q_{MI} + L_{eff} A_p \frac{2}{P} \omega_e. \tag{3.2.3}$$

3.3 Digital Control Analysis

The WCS TORVAD$^{\text{TM}}$ utilizes a micro-controller in order to observe the heart pump's operating performance and command control effort when necessary. Because of this, implementing a digital control scheme in the working simulation of the model allows for increased robustness of model analysis and dynamic performance. This also allows for micro-controller sampling frequency analysis to be done in order to assess the required sampling rate to avoid model instability.

3.3.1 Digital Control Scheme

One method of implementing digital (or discrete time) control is to use the zero-order hold (ZOH) method of control effort input, which holds the sample input constant throughout the discrete sample period[7]. In the case of the heart pump, the non-linear dynamic equations were evaluated at a time-scale of $\Delta t_c = 0.0001[s]$, while the digital controller took samples and held a constant effort value every

$\Delta t_d = 1/4800[s]$, where 4800 comes from the frequency of the micro-controller (4800 Hz).

Currently, a Proportional-Integral (PI) method of control of the BLDC motors is used within the TORVAD™, which is based on error with regard to stroke angle. PI control is beneficial for micro-controller implementation due to fact that the system dynamic equations are non-linear. Since PI control only takes into account the error of a given performance metric, no linearization or approximation is required to simulate and control the system. Thus, the PI control scheme can be used under the assumption that it is robust enough to handle the original nonlinear system.

A continuous PI controller will specify a pulse-width modulus (PWM) duty cycle as,

$$DutyCycle(t) = K_p e(t) + K_i \int_{t_0}^{t_f} e(\tau) d\tau. \tag{3.3.1}$$

In discrete form, the equivalent PI controller equation for each sample period iteration, k, takes the form

$$DutyCycle[k] = K_p e[k] + K_i T_s \sum_{n=0}^{k} e[n] \tag{3.3.2}$$

where K_p and K_i denote the gain values associated with the proportional and integral error values, respectfully, T_s is the sampling period equivalent to Δt_d, and e represents the error between the desired state value and the measured output. In this case, the error is the difference between desired angular position and actual angular position, or $e = \theta_{m,desired} - \theta_{m,actual}$.

This PI controlled duty cycle was evaluated each Δt_d using a proportional gain, K_p, of 300 [Duty/rad] and integral gain, K_i, of 150 [Duty/rad*s]. The results are shown below in Figure 3.2.

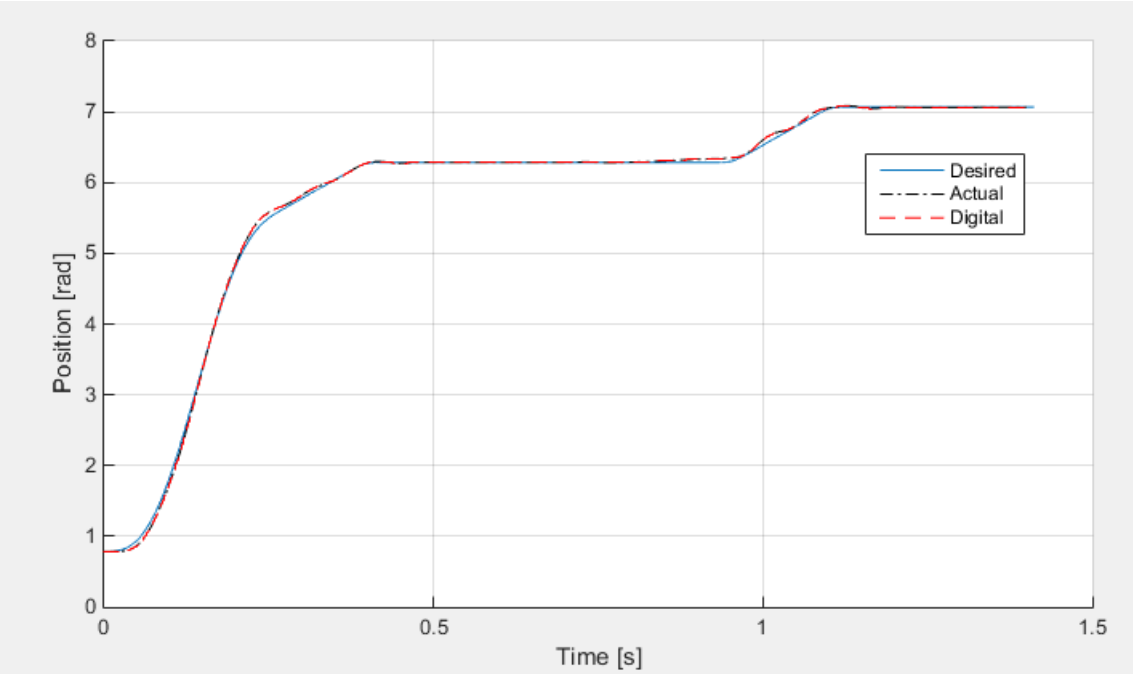

Figure 3.2: Position response to digital PI control at 4800 [Hz].

In this plot, the 'Desired' curve represents the predetermined trajectory that the PI controller references in order to solve for position error during each time step. The 'Digital' curve represents the zero-order hold position response, where each position is determined and held constant for each discrete time step, Δt_d. The 'Actual' curve represents how the position actually responds during the time between each discrete time step of the micro-controller.

Zooming in on the figure allows for a better interpretation of the zero-order hold method of digital control.

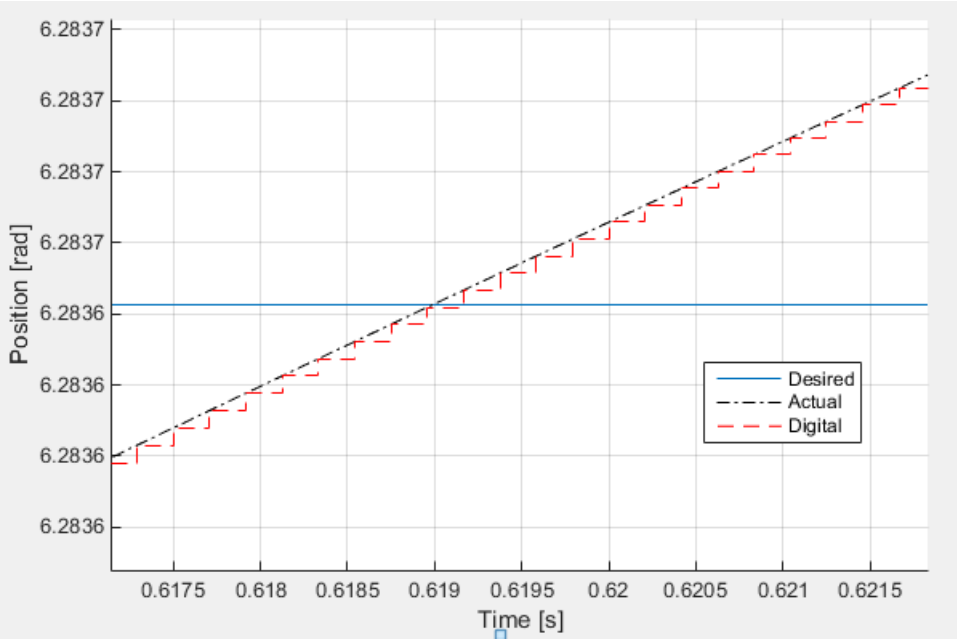

Figure 3.3: Zoomed view of position response to digital PI control at 4800 [Hz].

The visualization of 'Digital' versus 'Actual' curves is much clearer when looking at the zoomed position response. Due to the small discrete time step, Δt_d, the system can be controlled and kept stable. The corresponding control input, which is implemented through the use of the BLDC motor input duty cycle, is shown below in Figure 3.4.

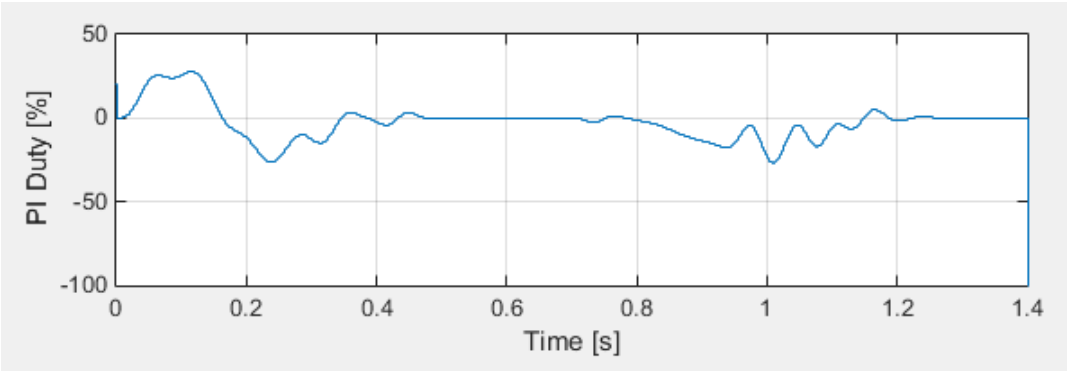

Figure 3.4: Control input response to digital PI control at 4800 [Hz]. Input duty cycle is limited between -100 and +100 percent.

Using a a discrete sampling period of $\Delta t_d = 1/4800[s]$, the average angular position error of the PI controlled system was 0.7 percent and the max error was 8 percent

which occurs at the beginning of the simulation as the actual system converges to the desired trajectory.

3.3.2 Micro-Controller Frequency Tests

As mentioned previously, the implementation of the digital PI control scheme to the full heart pump model allows for a sampling rate, or clock frequency, stability analysis to be performed. This analysis allows for the determination of the stable range of operating frequencies for the micro-controller board. It is important to note that lowering the operating frequency reduces the amount of power consumed by the micro-controller board. Therefore, there is a compromise between power consumption and system stability. Other measures, such as leakage, provide additional insight in micro-controller performance, but is out of the scope of work for this thesis.

Using the same PI gains as the previous section, instability was achieved at around the 320 [Hz] range ($\Delta t_d = 1/320[s]$). The resulting plot can be seen in Figure 3.5.

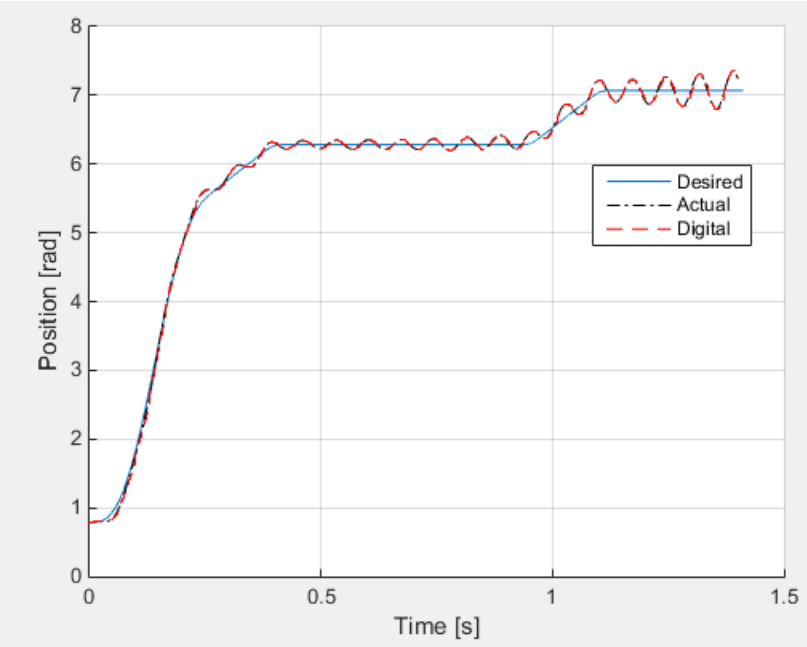

Figure 3.5: Position response to digital PI control at 320 [Hz].

It can be seen that the micro-controller is sampling the continuous system too slowly and cannot command control input fast enough to account for the continuous system dynamics. The system instability is much more apparent in the PI control

input plot which shows how the control input begins to oscillate as the system repeatedly applies overcompensated input. This oscillatory behavior of the control input is shown in Figure 3.6.

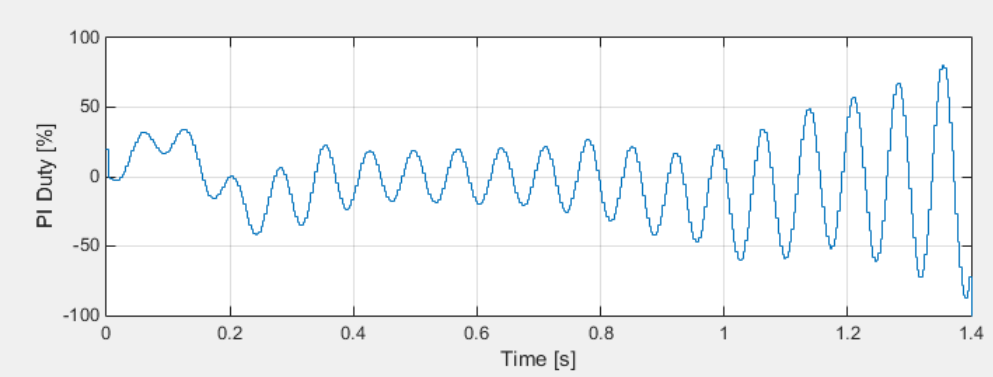

Figure 3.6: Control input response to digital PI control at 320 [Hz].

Compared to the initial control frequency of 4800 [Hz], a control frequency of 320 [Hz] causes the max angular position error to increase to 10 percent with the average error more than doubling at 1.5 percent.

In addition to the position error incurred by the slow sample rate of the microcontroller, the cardiovascular system also suffers in desired performance as shown below in Figure 3.7.

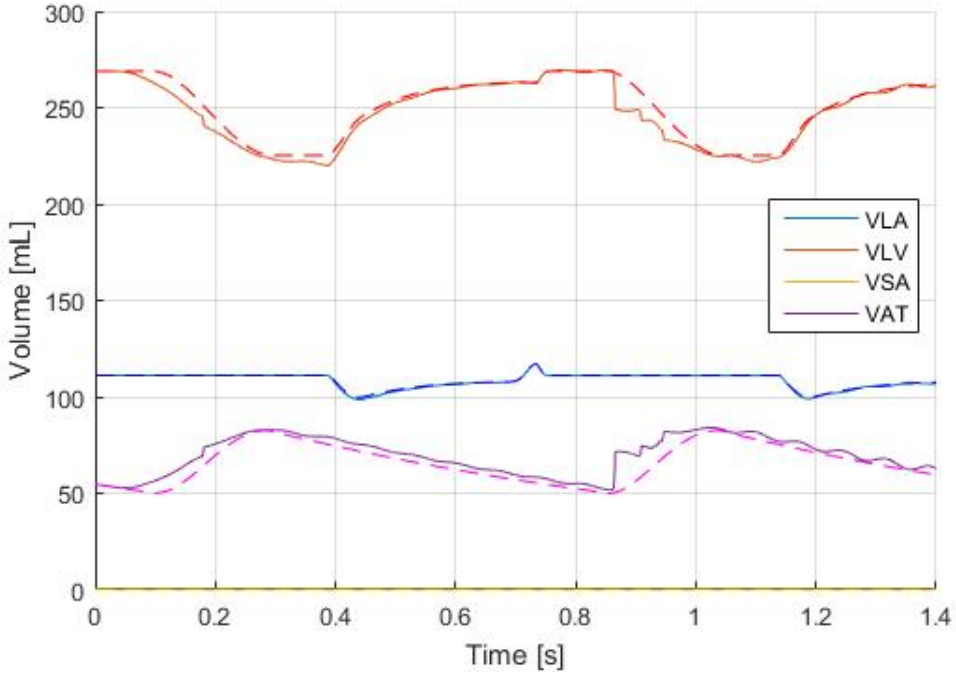

Figure 3.7: Cardiovascular system response to digital PI control at 320 [Hz].

Note the large perturbations in the volumes of both the left ventricle (VLV) and atrial tree (VAT) as compared to their ideal counterparts (shown by the dotted line).

3.4 Digital Control Summary

The digital, or discrete time, analysis provides a visualization of how the motor micro-controller is sampling and implementing control effort into the dynamic motor system. This visualization and analysis is useful in the motor design process for determining electronic and physical system requirements. For instance, if a micro-controller using a sampling frequency of 320 [Hz] was implemented within a heart pump implanted into a human patient, the large perturbations seen in Figure 3.7 could potentially be noticeable to a person equipped with the heart pump and put the individual at risk for other health concerns. By analyzing how the micro-controller reacts to the dynamics of the heart pump model, design considerations can be made to make the controller more robust while minimizing unnecessary costs, like excess power consumption.

As for the Digital Analysis results, it was determined that the micro-controller

should stay at a frequency of 4800 [Hz] in order to keep the average angular position error below 1% and the maximum position error (when initially converging) below 10%. The CVS system response to the next lowest applicable frequency, 2400 [Hz], showed minor perturbations[2]. Though they might be insignificant to the cardiovascular system, it was decided that eliminating all possible perturbations was the highest weighted priority, hence the selection of 4800 [Hz].

[2]The frequency of 2400 [Hz] was selected based on obtainable operating frequencies specified by WCS.

4. Optimal Control Methods

In this chapter, two methods of optimal control are introduced and evaluated. Section 4.1 formulates the dynamic heart pump system to be optimized. With the simplified heart pump system model fully defined, the next step in optimizing motor actuation was to define what the optimal solver would be trying to minimize or maximize. As stated in Chapters 1 and 3, the minimization of power was the primary focus of this thesis. Specifically, the optimal stroke trajectory for a single motor that minimizes motor power consumption. Sections 4.2, 4.3, and 4.4 discuss the Linear Quadratic Tracking and Hamiltonian approaches of optimal control, their respective simulation implementations, and how these optimization methods can be updated to focus on other performance criteria in the future.

4.1 Simplified Heart Pump Model

In order to evaluate the two chosen optimal control methods, an actual heart pump system model was required due to the time-variance of the CVS dynamic model. In order to accomplish this, a model of a test apparatus for the heart pump system was created. The reason for using this form of model is so that these methods could be initially tested on a test setup (a mock circulatory loop) to assess performance. Testing on a benchtop analog of the CVS is a standard approach in this field. This model makes the following assumptions about the relationship between the BLDC motor/pump and CVS systems.

1. The flow output of the BLDC motor/pump system does not induce significant dynamic effects within the cardiovascular system (i.e. CVS pressures at inlet and outlet of BLDC motor system are not affected by motor performance).

2. To simulate benchtop testing, the test load can be modeled as a parameterized flow resistance accompanied by cannula tube compliance.

A schematic of the simplified heart pump system is shown below.

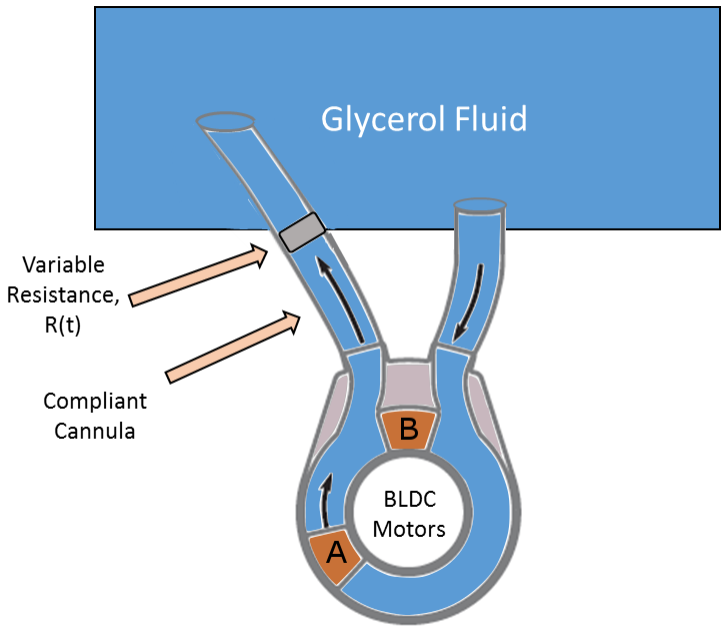

Figure 4.1: Schematic of benchtop test apparatus for evaluating optimal trajectory algorithms.

In order to determine the system dynamic state equations, a bond graph modeling approach was used. The bond graph for this experimental setup is shown in Figure 4.2.

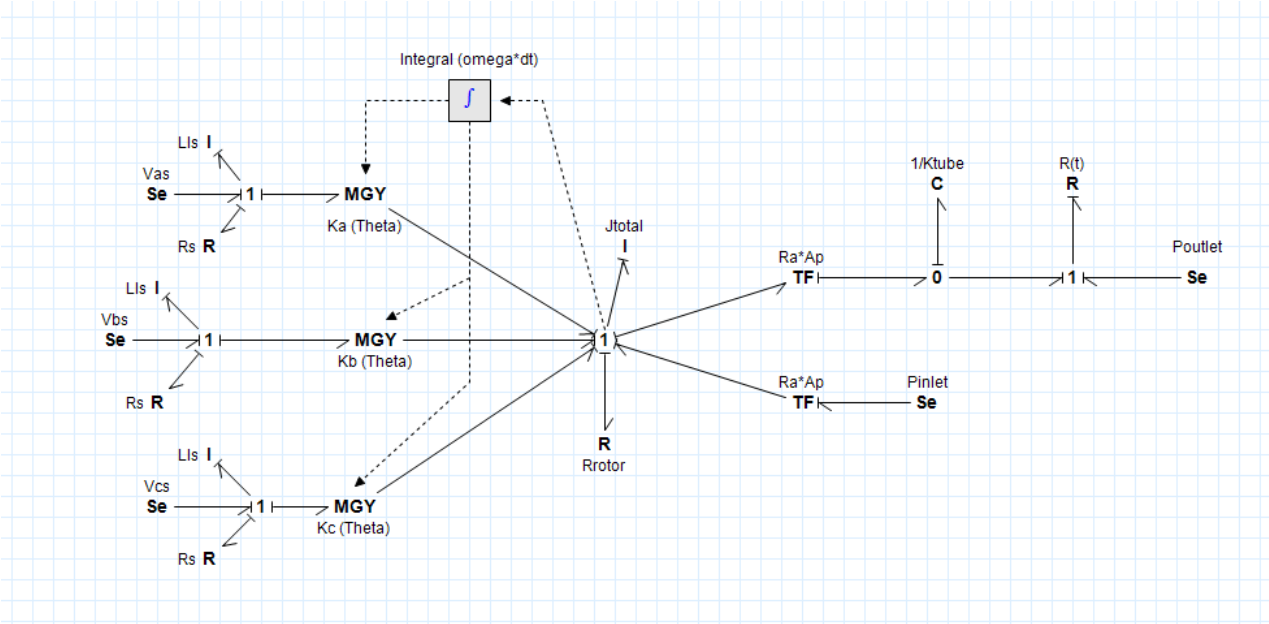

Figure 4.2: Bond graph representation of BLDC motor/pump/load test apparatus.

The bond graph includes five independent energy storing elements and one modulation parameter which is the integral of an inertial flow variable, therefore the system is made up of 6 total states. The mutual inductance between each of the three phases of the BLDC motor has been omitted for a simpler visual representation of the model.

The state vector of the simplified heart pump system, $X \in \mathbb{R}^6$, can be written as

$$X = \begin{bmatrix} \lambda_{as} & \lambda_{bs} & \lambda_{cs} & \omega_r & \theta_r & V_c \end{bmatrix}^T$$

where the introduction of state V_c is the volumetric expansion of the cannula tubing.

The dynamic equations for the experimental setup are identical to that of Section 2.1, except we may now introduce a load torque, τ_L, as

$$\tau_L = (L_{eff}A_p)^2(\frac{2\omega_r}{P})(R_{inlet} + R_{outlet}) - L_{eff}A_p(K_{tube}V_c + P_{inlet}) \tag{4.1.1}$$

where L_{eff} is the effective length of the rotational arm of the piston, A_p is the surface area of the piston face, P is the number of stator poles within the BLDC motor, R_{inlet} and R_{outlet} are the inlet and outlet flow resistances, respectively, K_{tube} is the hydraulic stiffness of the cannula, and P_{inlet} is the tank pressure at the inlet cannula.

To complete the model, the last dynamic equation for the volumetric expansion of the cannula is defined as

$$\dot{V}_c = L_{eff} A_p (\frac{2\omega_r}{P}) - \frac{K_{tube} V_c + P_{outlet}}{R_{clamp}} \tag{4.1.2}$$

where P_{outlet} is the known (input) tank pressure acting on the outlet cannula and R_{clamp} is the variable flow resistance within the outlet cannula.

4.2 Optimal Control Method 1: Linear Quadratic Tracking

This section details the implementation of the Linear Quadratic Tracking (LQT) method of optimal control [10]. An extension of the Linear Quadratic Regulator (LQR), which regulates all state values to zero, the LQT optimal control scheme instead regulates the difference between a desired and actual state value to zero. The optimal control solution is then a control law that drives states towards predetermined desired values. This method of optimal control was chosen due to its use of weighted gain matrices that drive the control system states and control input based on gain magnitude. This means admissible state and control input variations can be weighted separately, which allows for emphasis to be placed on tracking to desired state values while minimizing control input.

4.2.1 Linearization of Simplified LVAD System

In order to utilize the LQT optimal control method, the heart pump dynamic equations must first be reconstructed into a linear combination of states and inputs. Basic linearization techniques, such as the small perturbation method, cannot be utilized since the heart pump does not operate around a single equilibrium point. Instead, the heart pump operates around a known trajectory, which leads to the more intensive trajectory linearization method of linearization [8].

The trajectory linearization method utilizes Taylor expansion along multiple nominal trajectory points to replace the state vector, X, with a perturbation state, ΔX. The following equations define the trajectory linearization method.

The original time-invariant, nonlinear system is expressed as,

$$\dot{X}(t) = f(X(t), U(t)), \tag{4.2.1}$$

and the nominal, or known, system trajectory is given in a similar form by,

$$\dot{X}_N = f(X_N(t), U_N(t)). \tag{4.2.2}$$

We assume the motion of the nonlinear system is in the neighborhood of the nominal system trajectory. This is expressed as,

$$X(t) = X_N(t) + \Delta X(t). \tag{4.2.3}$$

The control input is also assumed to be in the neighborhood of the nominal control, which is expressed as,

$$U(t) = U_N(t) + \Delta U(t). \tag{4.2.4}$$

After Taylor expansion is applied to the nonlinear system about the nominal trajectory and input, the linearly approximated dynamic system is,

$$\Delta\dot{X}(t) = \frac{\partial f}{\partial X}(X_N, U_N)\Delta X(t) + \frac{\partial f}{\partial U}(X_N, U_N)\Delta U(t), \tag{4.2.5}$$

where $\frac{\partial f}{\partial X}$ and $\frac{\partial f}{\partial U}$ are both evaluated at the nominal trajectory points, (X_N, U_N), and represent the linear, state-space matrices $A(t)$ and $B(t)$, respectively.

The new linear system takes the form,

$$\Delta\dot{X}(t) = A(t)\Delta X(t) + B(t)\Delta U(t). \tag{4.2.6}$$

After $\Delta X(t)$ has been solved using the LQT method (described in the following section), the overall system performance is found using Equations 4.2.3 and 4.2.4 above.

4.2.2 Linear Quadratic Tracking Equations

The LQT method of optimal control requires a linear plant model, a weighted quadratic cost functional, and a reference state matrix. The linear plant model, or control system, is provided after linearization in Equation 4.2.6. The output of this linear system is the linear output matrix, Y, which (for the sake of simulation)

assumes all states can be measured[1]. The output matrix is expressed as,

$$Y = CX + DU = \mathbb{I}_{6x6}X. \tag{4.2.7}$$

The weighted quadratic cost functional for the infinite horizon LQT method of optimal control is defined by [10],

$$\begin{aligned} J(u) = \frac{1}{2}\Big[CX(t_f) - r(t_f)\Big]^T P\Big[CX(t_f) - r(t_f)\Big] + \\ \frac{1}{2}\int_{t_0}^{\infty}\Bigg(\Big[CX(t) - r(t)\Big]^T Q\Big[CX(t) - r(t)\Big] + \\ U(t)^T RU(t)\Bigg)dt, \end{aligned} \tag{4.2.8}$$

where the running cost weight matrices for the states and control input are Q and R, respectively, P is the terminal cost weight matrix, and $r(t)$ is the desired state value tracking matrix. (Note: $r(t_f)$ denotes the desired state value tracking matrix evaluated at the final time, t_f). The weighting terms Q and P are positive semi-definite, symmetric matrices and R is a positive definite and symmetric matrix.

The infinite horizon LQT optimal full-state, affine feedback control input is defined by,

$$U = -K(\infty)X + R^{-1}B^T\nu(\infty), \tag{4.2.9a}$$

where $K(\infty)$, the steady-state Kalman gain matrix, is defined by,

$$K(\infty) = R^{-1}B^T S(\infty), \tag{4.2.9b}$$

where $S(\infty)$, the solution to the Algebraic Riccati Equation (ARE), is solved using,

$$0 = A^T S(\infty) + S(\infty)A - S(\infty)BR^{-1}B^T S(\infty) + C^T QC, \tag{4.2.9c}$$

and where the tracking equation (represented by state variable ν) solution is found

[1]Setting the output matrix C equal to a 6x6 Identity matrix, rather than a 1x6 zero matrix with the θ_r element equal to 1, allows for other optimization opportunities in the future. Each state can be tracked according to the LQT cost functional, which can be updated and utilized at a later time if desired.

using the equation,

$$0 = (A - BK(\infty))^T \nu(\infty) + C^T Q r(t). \tag{4.2.9d}$$

The infinite horizon LQT problem was chosen due to the time varying, linear system A and B matrices. Each of these matrices are defined based on the nominal state trajectory at a given point in time, therefore continuous time Riccati and Tracking equation solutions would need updated A and B matrix values at each moment in time used in the ODE solver. In order to avoid unwieldy saved matrices, the infinite horizon LQT problem allows for the ARE and Tracking equation to be solved at one iteration in time. The assumption required for this method, however, is that the final solver time, t_f, is sufficiently large so that the control system has time to reach the desired state trajectory after starting at time t_0. This assumption is acceptable since the desired state tracking values used in Chapter 5 of this thesis can be met easily within the given time frame of $t \in [t_0, t_f]$.

With all LQT components defined, the simulation testing is conducted in MathWorks' dynamic analysis software MATLAB. The time variance of the linearized A and B matrices require an iteration based approach where the optimal solution is determined for each time-step δt according to the procedure below.

1. For the entire forward time span of $t = [t_0 : \delta t : t_f]$ where $t_f > t_0$ and δt is the size of each time step:

   Evaluate and save all $A(t_i)$ and $B(t_i)$ matrices based on nominal state trajectory at each i^{th} time iteration $t_i \in [t_0, t_f]$

2. The optimal solution must be solved backwards in time and iteratively. For each j^{th} iteration in the backward time span of $t_b = [-t_f : \delta t : -t_0]$ where $t_j \in [-t_f, -t_0]$:

   Set tracking matrix, $r(t_j)$, based on the difference in the j^{th} iteration between desired final state trajectory and current nominal state trajectory (e.g. The tracking value for the j^{th} iteration of angular position is defined as $r(t_j) = \theta_{desired}(t_f) - \theta_{nominal}(t_j)$)

3. Solve steady-state Riccati and steady-state tracking equations (Equations 4.2.9c and 4.2.9d, respectively) using $A(t_j)$, $B(t_j)$, and $r(t_j)$, then save. Note: The

$A(t)$ and $B(t)$ matrices in Step 1 correspond to iterations forward in time, therefore $A(t_j)$ and $B(t_j)$ must be pulled backwards - starting from the $A(t_f)$ and $B(t_f)$ values towards the initial time values $A(t_0)$ and $B(t_0)$.

With the Riccati and tracking equation solutions, as well as the linear system matrices $A(t)$ and $B(t)$, it is possible to determine the optimal LQT state trajectory output by simulating the system in Equation 4.2.6 using the optimal control input provided in Equation 4.2.9a.

4. Go back to forward time where $t = [t_0 : \delta t : t_f]$:

   Use ODE solver in MATLAB to solve Equation 4.2.6 for each k^{th} iteration of $t_k \in [t_0, t_f]$. Reminder: The optimal control problem simulation is now complete, however Equation 4.2.3 must be used to define the fully optimized control system.

4.2.3 LQT Limitations

After implementing the LQT optimal control method, it was observed that the optimal solution was heavily influenced by the nominal trajectory. In fact, the LQT method is very useful for slightly adjusting a nominal curve to optimize performance according to the performance criteria within the cost functional. However, the goal of this thesis is to determine the overall optimal trajectory from initial condition, X_0, to a desired terminal condition, X_f, without providing any guidance to the optimal solver other than the cost functional.

Another limitation was that the active power of the control system could not be explicitly weighted. According to the linear quadratic cost functional, only the states, control input, or linear combination of the two can be influenced directly. Therefore, the voltage input to the system could be weighted, but not the product of instantaneous current and voltage. Though one component of power can be influenced, this does not guarantee optimality.

The last limitation of the LQT optimal control method was that the terminal state constraints were soft constraints rather than hard constraints. In other words, the LQT control forced the control system near the desired terminal state values, but would not guarantee that the states would be equivalent to the desired at the final time. Implementing a solver with hard terminal constraints would force the system to reach and stay at the desired state values by the end of the simulation.

4.3 Optimal Control Method 2: Hamiltonian Approach

Due to the limitations in LQT as described in Section 4.2.3, a new optimal control approach was evaluated. A Hamiltonian approach to optimal control of continuous-time systems was evaluated using the Steepest Descent method of simulation implementation[10, 11].

4.3.1 State Augmentation

The Steepest Descent method is a numerically iterative optimization approach. Upon implementation using the three-phase control system defined in Sections 2.1 and 4.1, the solver had great difficulty converging to a solution. Believing the oscillatory behavior of the three-phase system to be the root cause, the control system was transformed from a three-phase, machine variable reference frame to a rotor reference frame (dq0-space) by utilizing the Park's Transformation[5]. Thus the oscillatory nature of the state equations was transformed into a non-oscillatory configuration, which allowed the optimization approach to converge while keeping the core state relationships of the control system intact.

The augmented state matrix of the simplified heart pump system, $X \in \mathbb{R}^6$, can be written as,

$$X = \begin{bmatrix} I_{qs} & I_{ds} & I_{0s} & \omega_r & \theta_r & V_c \end{bmatrix}^T,$$

where the first three state elements are now the currents of each transformed phase. The updated dynamic equations for the dq0 currents take the following form,

$$\dot{I}_{qs} = \frac{1}{L_q}\Big(V_{qs} - \omega_r L_d I_{ds} - \omega_r \lambda_m^{'} - R_s I_{qs}\Big), \tag{4.3.1a}$$

$$\dot{I}_{ds} = \frac{1}{L_d}\Big(V_{ds} + \omega_r L_q I_{qs} - R_s I_{ds}\Big), \tag{4.3.1b}$$

$$\dot{I}_{0s} = \frac{1}{L_0}\Big(V_{0s} - R_s I_{0s}\Big), \tag{4.3.1c}$$

where

$$L_q = L_d = L_{ls} + \frac{3}{2}L_{ms}, \tag{4.3.1d}$$

and

$$L_0 = L_{ls}. \tag{4.3.1e}$$

The latter three state elements' dynamic equations remain the same as in Sections 2.1 and 4.1, but with an updated electromagnetic drive torque, τ_e, expressed as,

$$\tau_e = \Big(\frac{3}{2}\Big)\Big(\frac{P}{2}\Big)\Big(\lambda_m^{'} I_{qs} + (L_d - L_q) I_{qs} I_{ds}\Big). \tag{4.3.2}$$

The updated control input to the BLDC motor system is the voltage duty cycle translates into a singular voltage input, $U \in \mathbb{R}^1$, shown as,

$$U(t) = V_s. \tag{4.3.3}$$

The corresponding voltages for each dq0 phase are,

$$V_{qs} = \sqrt{2} V_s cos(\phi_v) \approx \sqrt{2} V_s, \tag{4.3.4a}$$

$$V_{ds} = -\sqrt{2} V_s sin(\phi_v) \approx 0, \tag{4.3.4b}$$

and

$$V_{0s} = 0 \tag{4.3.4c}$$

with ϕ_v representing the phase angle between the commutation angle for the original V_{as} component and the actual angular position of the q-axis attached to the rotor. Since the implemented commutation scheme linearly interpolates between each of the 96-point sinusoidal commutation table position, ϕ_v is approximately zero for all time.

4.3.2 Hamiltonian Approach Equations

The Hamiltonian of a continuous, nonlinear optimal control system is defined by,

$$H(t, x, u) = L(t, x, u) + \lambda^T f(t, x, u), \tag{4.3.5a}$$

where $L(t, x, u)$ is the Lagrangian, or the running cost of the cost functional, $f(t, x, u)$ is the nonlinear control system, and λ is a $[n \times 1]$ matrix of Lagrange multipliers where n is the number of states in $f(t, x, u)$. Each Lagrange multiplier in λ is referred to as a costate for the remainder of this thesis.

As stated previously, the LQT method of optimal control could not explicitly

weight active power in the cost functional. The Hamiltonian approach, however, can implement nonlinear cost functional terms meaning an active power term can be added to the cost functional. The updated Lagrangian, or running cost, of the cost functional is,

$$\begin{aligned} L(t,x,u) = \frac{1}{2}\int_{t_0}^{t_f} \Bigg(\Big[CX(t) - r(t)\Big]^T Q \Big[CX(t) - r(t)\Big] + \\ \frac{3}{2}\gamma(I_{qs}(t)V_{qs}(t) + I_{ds}(t)V_{ds}(t) + 2I_{0s}(t)V_{0s}(t)) + \\ \Big[CX(t) - r(t)\Big]^T P \Big[C\dot{X}(t)\Big] + \\ U(t)^T R U(t) \Bigg) dt. \end{aligned} \tag{4.3.5b}$$

The following three adjustments have been made to the running cost functional in Equation 4.3.5b versus the integral portion of Equation 4.2.8.

1. The running cost is now evaluated in a fixed-time format where $t \in [t_0, t_f]$
2. A nonlinear active power equation has been added in order to explicitly weight instantaneous active power.
3. The terminal cost function, or non-integral portion of Equation 4.2.8, has been placed inside the integral, effectively coercing the soft constraints to be much more rigid based on the elements within the matrix P.

Adjustment 1 eliminates the assumption that the control system has plenty of time to reach the desired state values, as in the infinite horizon LQT control scheme. The system either has enough time or the optimal solution output will show that it does not. Adjustment 2 allows for a weighted balance to be struck between reaching the desired trajectory faster (larger Q element magnitudes) and minimizing power consumption (larger γ magnitudes). Lastly, adjustment 3 better ensures that the control system reaches the desired state values by the end time of the simulation.

The state, costate, and optimal control input equations are derived from the Hamiltonian. Though previously known, the state equations are determined by

$$\dot{X} = \frac{\partial H}{\partial \lambda} = f(t,x,u) \qquad \forall t \geq t_0 \tag{4.3.6}$$

The costate equations are determined using the partial derivative of the Hamiltonian with respect to the states

$$-\dot{\lambda} = \frac{\partial H}{\partial X} = \frac{\partial f^T}{\partial X}\lambda + \frac{\partial L}{\partial X} \qquad \forall t \leq t_f \tag{4.3.7}$$

And the optimal control input comes from the Stationarity condition where U(t) is determined by setting the partial derivative of the Hamiltonian with respect to the input equal to zero.

$$0 = \frac{\partial H}{\partial U} = +\frac{\partial L}{\partial U} + \frac{\partial f^T}{\partial U}\lambda \tag{4.3.8}$$

4.4 Optimal Control Summary

The Linear Quadratic Tracking method of optimization was chosen based on its versatility with linear and nonlinear systems, as well as its relevance in current optimal control literature [9, 10, 11]. However, the LQT method was not a preferable method of optimization for this dynamic system due to its requirement of a nominal trajectory information. This information proved too influential for the optimal solver, which caused the output solutions to be incorrectly biased. Because of this, another method was implemented using the Hamiltonian Approach and the Steepest Descent method for simulation data convergence. The Hamiltonian approach is most beneficial in its ability to add nonlinear or non-quadratic cost functions within the Lagrangian. This allowed for weighting factors to be placed on any desired minimization or maximization equations provided in the cost function, which was exactly the case for instantaneous power consumption within the motor system. By weighting both instantaneous power consumption and tracking error between desired and actual stroke trajectory, the simulation was coerced into determining a solution that minimized both parameters. This versatility of the Hamiltonian Approach allows for more optimality constraints to be examined in the future, either in conjunction with power consumption minimization or assessed separately. The simulation results from applying both LQT and the Hamiltonian approach to the simplified heart pump system described in Section 4.1 are discussed in the next chapter.

5. Results

The following sections detail the results of both optimization techniques described in Chapter 4 and the methods by which they were implemented for simulation. All simulations and figures were generated using MathWorks' MATLAB software.

Each optimization technique provides an optimal stroke trajectory which minimizes BLDC motor power consumption for a single stroke of motor actuation. The optimal trajectory has a terminal constraint for the stroke angle, $\theta_m(t_f)$, which is set at 315 [deg] or 5.498 [rad]. The optimal solvers also have input voltage constraints that limit the control input to between $\pm$ 14.9 [V]. The stroke angle requirements are based on geometric properties of the prototype WCS TORVAD$^{\text{TM}}$ and the input voltage requirement is the corresponding duty cycle span of $Duty \in [-100, 100]\%$.

5.1 LQT Method Results

As stated in Section 4.2, the LQT method of optimization requires some preliminary state information in the form of nominal state trajectories (X_N) and control input values (U_N) over the given simulation time span. Since the focus of the optimization was to determine the optimal stroke trajectory, multiple candidates for nominal stroke trajectory were developed and tested. See Appendix for system parameter values table and flowchart of entire LQT simulation implementation.

5.1.1 Implementing Nominal Trajectories

A total of five nominal trajectory candidates were tested using the LQT method of optimal control. Two of these trajectories were developed (and are currently in use in the actual prototype heart pump system controller) by WCS. The trajectories, starting with the two WCS curves, are listed below with their shorthand designation in parentheses.

- WCS Asynchronous Curve (WCS Async): Designed so that the derivative is nonzero at all times, the WCS Async curve is the only nominal curve that starts at the initial stroke angle of $\theta_m(t_0) = 34[deg] = 0.5934[rad]$. The final desired stroke angle remains the same, therefore implementation in the optimal control simulation is a simple update of the initial conditions.

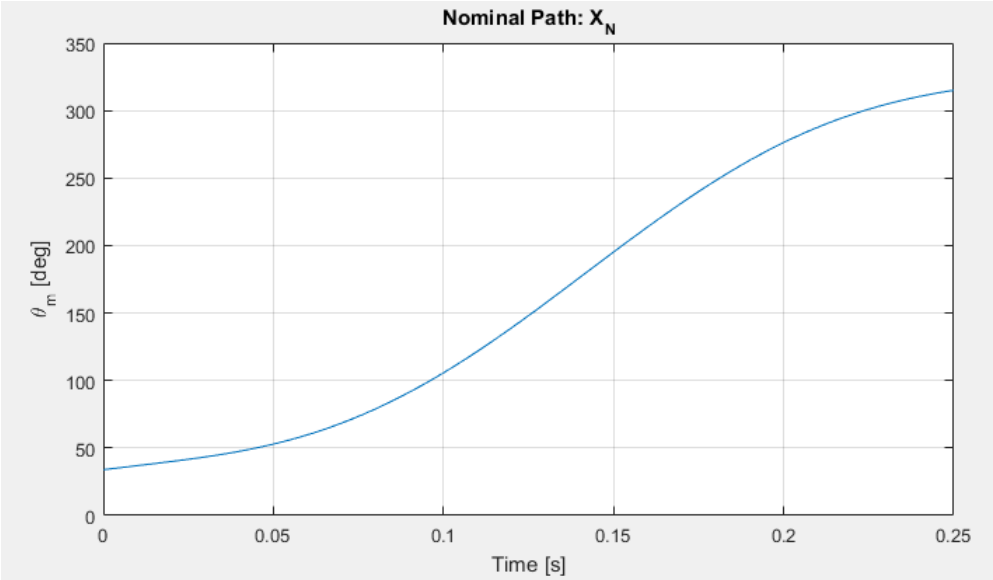

Figure 5.1: WCS asynchronous stroke angle trajectory.

- WCS Synchronous Curve (WCS Original): Similar to the WCS Async curve, the WCS Original curve was designed with the intent to drive the motors smoothly from one zero velocity position to the next, without any large spikes in velocity in between. The initial stroke angle of this curve, and all trajectories below, is equivalent to $\theta_m(t_0) = 45[deg] = 0.7854[rad]$.

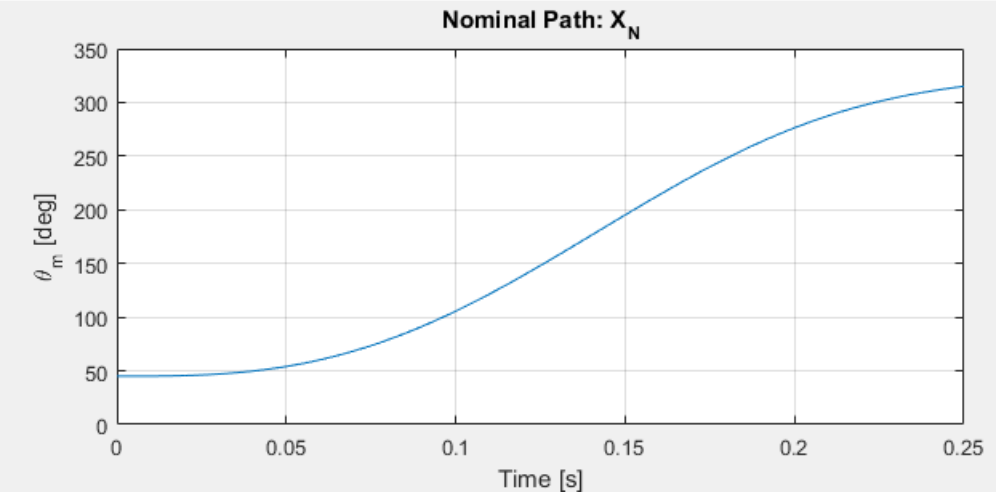

Figure 5.2: WCS synchronous stroke trajectory.

- Linear Curve (Linear): A linear trend was proposed due to its constant derivative and the knowledge that the motor controller could force such a trend without any issues. The linear curve is defined by the equation $\theta_m = \alpha t + \theta_m(t_0)$ [deg] where $\alpha = \frac{315-45}{t_f}$ and $\theta_m(t_0) = 45$ [deg].

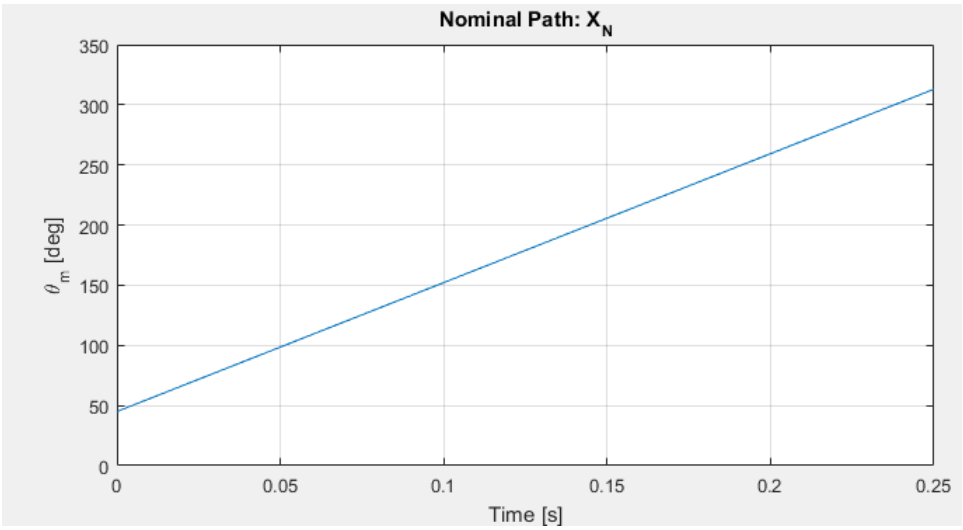

Figure 5.3: Linear stroke trajectory.

- Square-root Curve (Sqrt): The square-root trend was proposed to emulate a path that attempted to reach the terminal position much faster than that of the WCS Async or WCS Original curves. The trend was designed to represent

an overdamped system reacting to an input step response and is defined by the equation $\theta_m = \beta\sqrt{t} + \theta_m(t_0)$ [deg] where $\beta = 530$ $[\frac{deg}{\sqrt{s}}]$ and $\theta_m(t_0) = 45$ [deg].

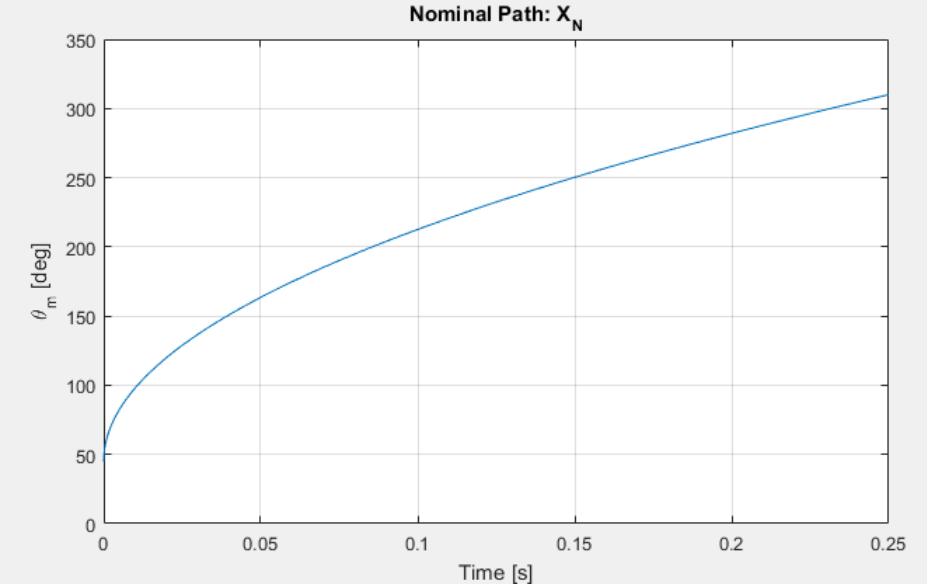

Figure 5.4: Square-root stroke trajectory.

- Exponential Curve (Exp): The exponential trend was evaluated purely as the antithesis of the square-root trend, causing the system to reach the desired terminal position at a later time with a larger velocity near the end. This curve is defined by the equation $\theta_m = e^{\gamma t} + \theta_m(t_0)$ [deg] where $\gamma = 4ln(271)$ $[\frac{1}{s}]$ and $\theta_m(t_0) = 44$ [deg].

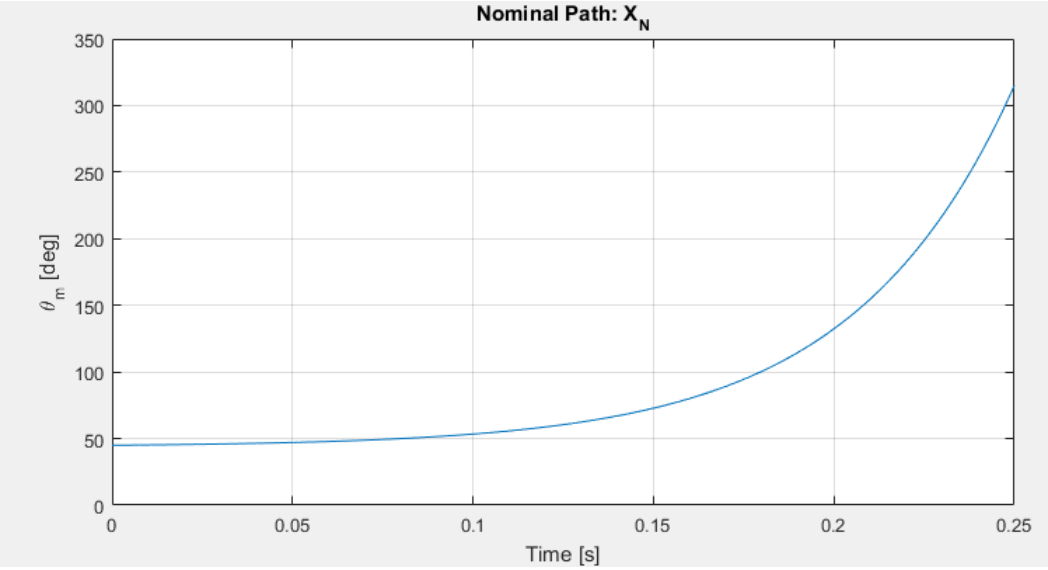

Figure 5.5: Exponential stroke trajectory.

The nominal stroke trajectory candidates are just one state within the entire nominal state matrix, X_N, however. In order to implement each of these candidate trajectories into the optimal control simulation, all other nominal state information was required (see Equations 4.2.5 and 4.2.6). To determine all nominal state trajectory information, a simulation file was developed that numerically solved the nonlinear control system using a PID controlled duty cycle that weighted the error between nominal stroke angle and actual stroke angle. The equation for the PID controlled duty cycle, similar to that of 3.3.1, is defined as

$$DutyCycle(t) = K_p e(t) + K_d \dot{e}(t) + K_i \int_{t_0}^{t_f} e(\tau) d\tau \tag{5.1.1a}$$

where

$$e(t) = \theta_{m,nominal}(t) - \theta_{m,simulation}(t). \tag{5.1.1b}$$

The PID control gains were determined through the Ziegler-Nichols Method of tuning and then adjusted heuristically based on desired steady-state error ($e_{SS} \leq 2.5\%$) and settling time ($t_s \leq 0.01$ s) [7].

By implementing this PID controlled simulation, all nominal state and control information[1] can be found for the stroke trajectory candidate, such as the WCS Async or Linear curves. The state information is then used at each moment in simulation time as a reference to linearize the nonlinear system according to Equation 4.2.5. An example of the PID controlled system output is shown below for the WCS Async stroke curve.

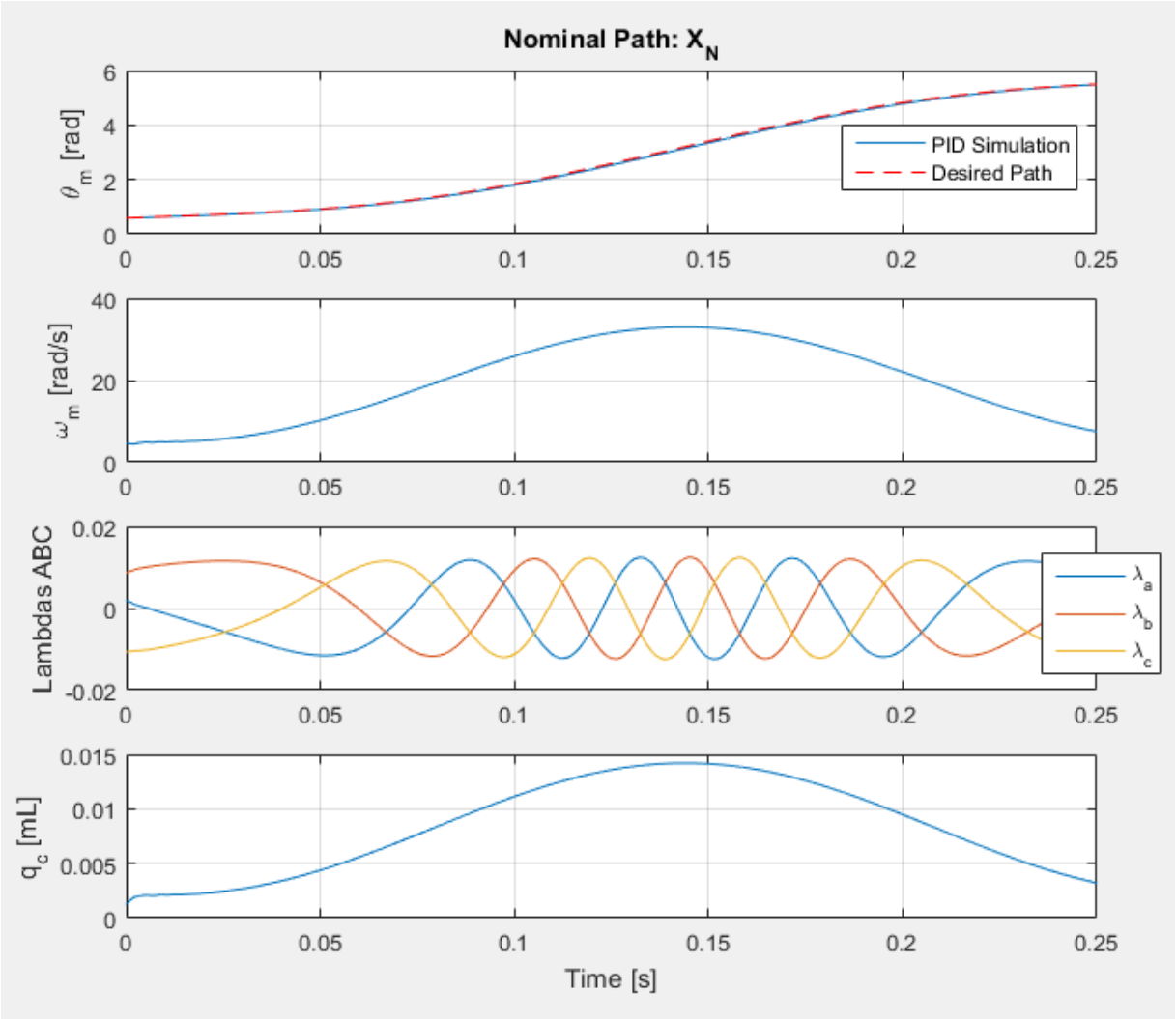

Figure 5.6: Full nominal state trajectory associated with WCS Async stroke curve.

The first subplot in Figure 5.6 shows the recreation of the WCS Async path from the PID controlled simulation. Each following subplot shows the state responses of

[1]Nominal state trajectory, $X_N(t)$, and control input, $U_N(t)$, information as defined in Section 4.2.1

the other states within the system. These state trends now complete the nominal state vector, $X_N(t)$, as defined in Section 4.2.1. With the PID simulation output path within acceptable error bounds (error $\leq 2.5\%$), the state output from the PID simulation was deemed appropriate for use as the nominal state trajectory.

The control input, which is a PID controlled duty cycle, to force the control system to follow the WCS Async curve is shown below. This control input trend makes up the nominal control vector, $U_N(t)$, as defined in Section 4.2.1. The corresponding voltage associated with the controlled duty cycle is shown as well.

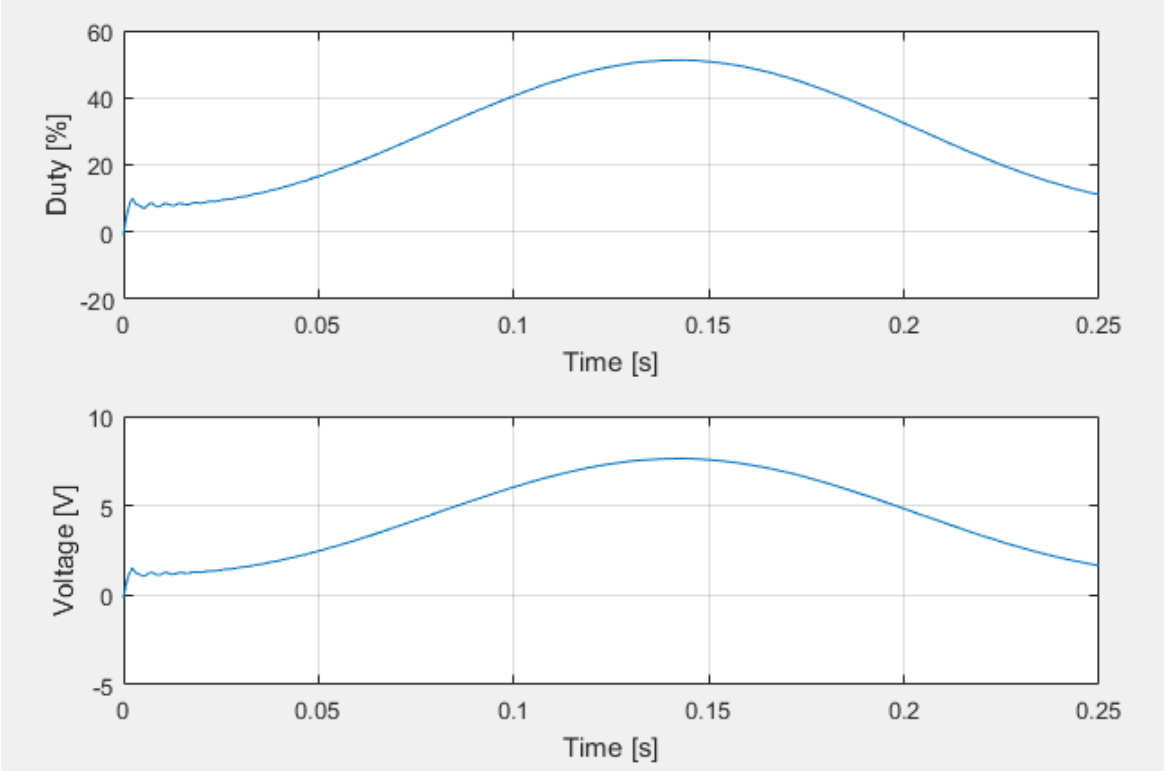

Figure 5.7: Nominal control input trajectory associated with WCS Async stroke curve.

For the remainder of this section, the LQT optimal control method will use the WCS Async curve and the associated nominal state information shown in Figures 5.6 and 5.7.

5.1.2 LQT Optimal Trajectory Output

With the nominal system trajectory determined ($X_N(t)$ and $U_N(t)$), the LQT method of optimal control was applied using the approach described in Section 4.2. The weighting matrices chosen for the simulation are shown below.

The terminal and running cost weighting matrices are defined as

$$P = Q = \begin{bmatrix} 0 & 0 & 0 & 0 & 0 & 0 \\ 0 & 0 & 0 & 0 & 0 & 0 \\ 0 & 0 & 0 & 0 & 0 & 0 \\ 0 & 0 & 0 & 0.1L_\omega & 0 & 0 \\ 0 & 0 & 0 & 0 & 10L_\theta & 0 \\ 0 & 0 & 0 & 0 & 0 & 0 \end{bmatrix} \tag{5.1.2a}$$

where $L_\theta = 0.0001\frac{kg^2}{J^2}$ and $L_\omega = 0.0001\frac{kg^2s^2}{J^2}$ are normalization factors that allow for the magnitudes of the running cost weights and control input weights to be directly compared. For example, the weight of 10 in the $Q(5,5)$ position emphasizes $100\times$ more concern over the admissible state performance than that of the weight in the $Q(4,4)$ position of 0.1.

The control input weight magnitude is

$$R = 0.1L_U \tag{5.1.2b}$$

where the normalization factor $L_U = 1\frac{J}{A*s}$.

The reference vector, $r(t)$, which needs to be updated at each time step, is defined as

$$r(t) = \begin{bmatrix} 0 \\ 0 \\ 0 \\ 0 \\ (\frac{P}{2})\Big(\theta_m(t_f) - \theta_{m,Async}(t)\Big) \\ 0 \end{bmatrix} \tag{5.1.2c}$$

where $\theta_m(t_f)$ is the final stroke position ($t = t_f$) and $\theta_{m,Async}(t)$ is the nominal stroke angle reference (WCS Async curve) at each iteration in time. Though each of the nominal trajectories are provided in terms of stroke position, the control system equa-

tions stated in Section 2.1 require electrical angular position for simulation. Therefore, the multiplication factor of $\frac{P}{2}$ has been added to the reference vector equation to transform the reference error to the correct domain.

The simulation output, as defined by Equation 4.2.5, for these weighting matrices is shown in Figure 5.8 below.

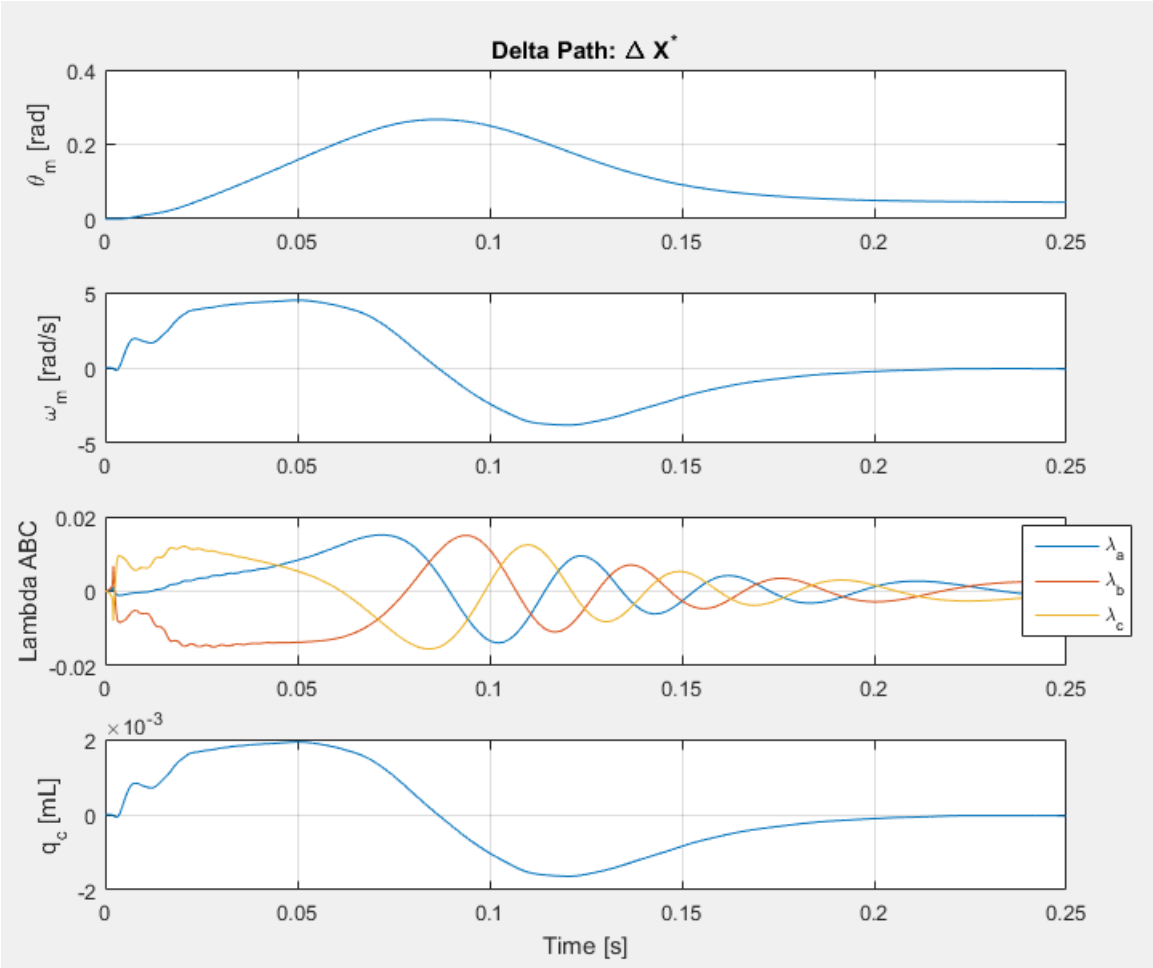

Figure 5.8: LQT control admissible state trajectories.

The corresponding admissible control input, ΔU, for the LQT control scheme is provided in Figure 5.9.

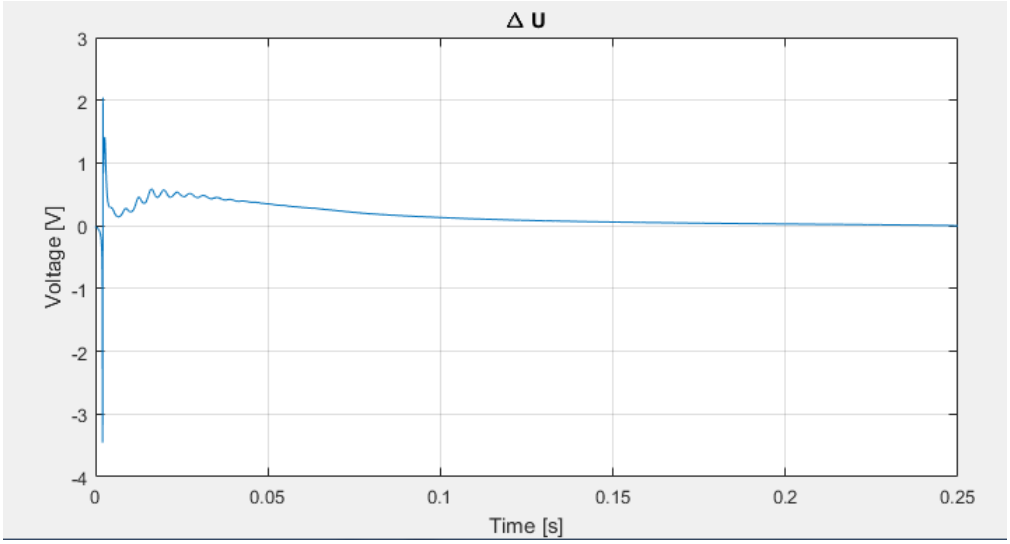

Figure 5.9: LQT control admissible control input trajectory.

Note the perturbations near the beginning of the optimal solution. These perturbations are due to the iterative linear approximation of the control system in the simulation and the infinite horizon assumptions. Decreasing the time-step helps mitigate these perturbations, but the overall trend (once smoothed) remains the same. Therefore, the current time-step was kept in order to lower numerical solver time.

Referring back to Equations 4.2.3 and 4.2.4, the optimized control system is found.

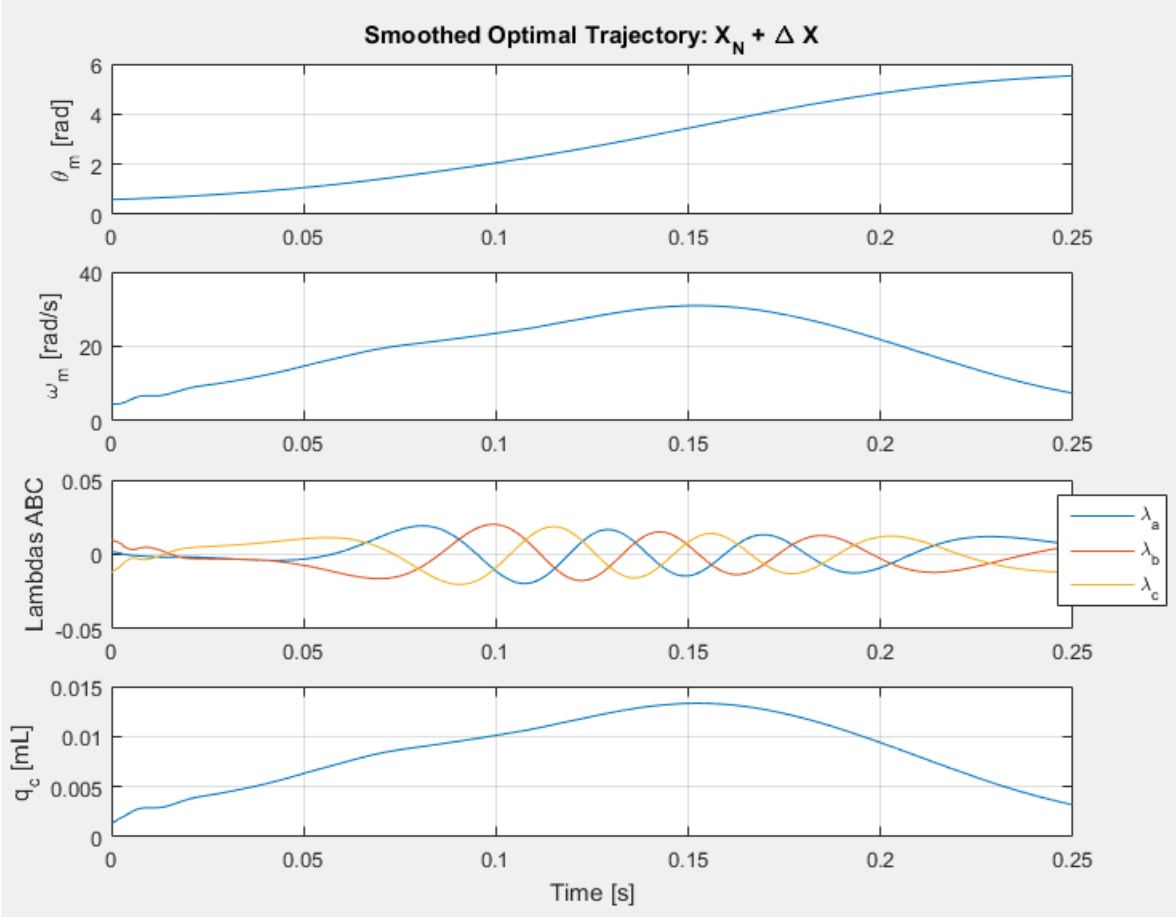

Figure 5.10: LQT control optimal state trajectories.

The corresponding control input trajectory can be seen in Figure 5.11.

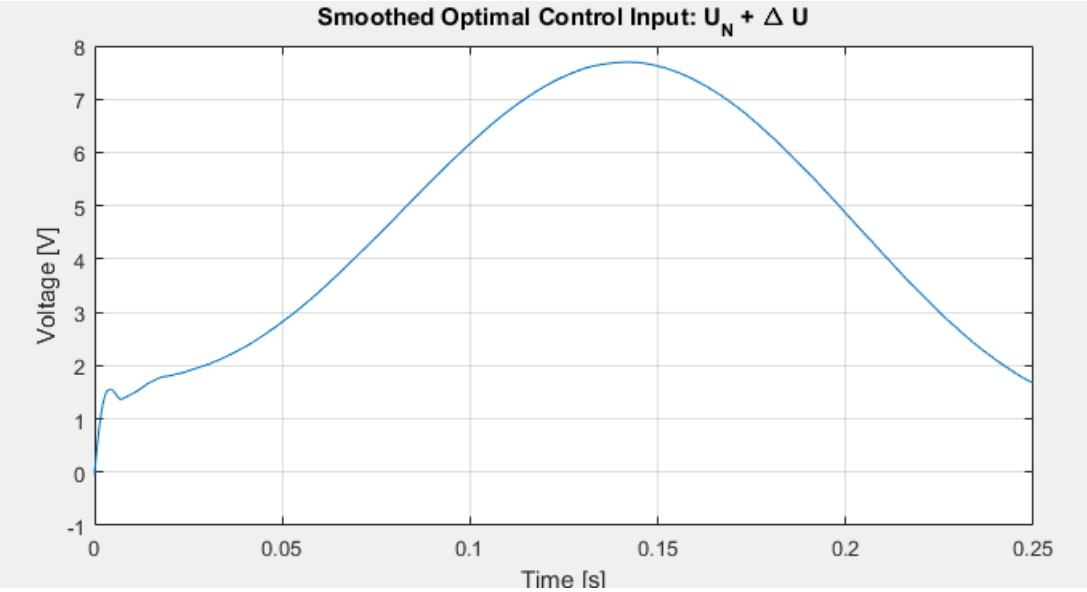

Figure 5.11: LQT control optimal control input trajectory.

Once the LQT simulation was complete, the cost functional of both the nominal and optimal systems were tallied and compared. This process was completed for each of the five candidate nominal trajectories discussed in Section 5.1.1 and tabulated.

Curve	Performance Index	Mean Power Consumed [W]	Mean Power Lost [W]	Mean Drive Power [W]	Efficiency [%]	Avg Flow [L/min]	% Power Drain Difference
WCS Async Nom	14.198	5.241	1.030	4.211	80.35	7.758	-7.26
WCS Async Opt	13.160	4.861	0.950	3.912	80.47	7.828	
WCS Original Nom	13.982	5.158	1.017	4.141	80.28	7.449	-3.73
WCS Original Opt	13.459	4.966	0.973	3.993	80.42	7.519	
Linear Nom	10.199	3.765	0.746	3.019	80.19	7.368	2.33
Linear Opt	10.384	3.853	0.754	3.099	80.43	7.449	
Sqrt Nom	18.164	6.790	1.354	5.435	80.05	7.317	1.72
Sqrt Opt	18.167	6.906	1.366	5.540	80.22	7.478	
Exp Nom	22.829	8.285	1.615	6.670	80.50	6.333	-14.87
Exp Opt	19.599	7.053	1.380	5.673	80.43	6.341	

Table 5.1: Optimal solution comparisons for each of the five candidate nominal trajectory curves discussed in Section 5.1.1

The columns of this table represent:

- Curve $\equiv$ Candidate reference trajectories and their optimized counterparts
- Performance Index $\equiv$ Evaluated cost functional value

- Mean Power Consumed ≡ Average power required from an external power source through the product of voltage and current of each phase ($P = V_{as}I_{as} + V_{bs}I_{bs} + V_{cs}I_{cs}$)
- Mean Power Lost ≡ Average power lost in the form of heat through the product of phase resistance and the square of current for each phase ($P = I_{as}^2R_s + I_{bs}^2R_s + I_{cs}^2R_s$)
- Mean Drive Power ≡ The difference between Mean Power Consumed and Mean Power Lost. This is the power that reaches the inertial system.
- Efficiency ≡ Percentage of Mean Drive Power over Mean Power Consumed
- Average Flow ≡ Average output flow provided by the piston
- Percent Power Drain Difference ≡ Comparison of the Mean Power Consumed column between the nominal and optimal trajectory output. A negative difference means that power consumption was lowered, hence the green shading. A positive difference means that power consumption was increased, hence the red shading.

From this table it can be seen that the LQT optimal control scheme helped minimize power consumption of three of the five candidate trajectories. The trajectory with the least power consumption, however, was the nominal Linear curve, which the LQT control scheme could not enhance.

5.2 Hamiltonian Approach Results

As stated previously, the Hamiltonian approach does not require any nominal trajectory information. Therefore, the only requirements for simulation are system parameter values (see Appendix) and determination of weighting constants and matrices.

The running cost weighting matrices are defined as

$$P = \begin{bmatrix} 0 & 0 & 0 & 0 & 0 & 0 \\ 0 & 0 & 0 & 0 & 0 & 0 \\ 0 & 0 & 0 & 0 & 0 & 0 \\ 0 & 0 & 0 & 0.1 & 0 & 0 \\ 0 & 0 & 0 & 0 & 200 & 0 \\ 0 & 0 & 0 & 0 & 0 & 0 \end{bmatrix} \tag{5.2.1a}$$

where the matrix P acts as a terminal constraint forcing matrix, which drives ω_r to zero and θ_r to a desired electrical angle by the final time.

The Q matrix dictates the speed at which the control system converges to the desired trajectory and is defined as

$$Q = \begin{bmatrix} 0 & 0 & 0 & 0 & 0 & 0 \\ 0 & 0 & 0 & 0 & 0 & 0 \\ 0 & 0 & 0 & 0 & 0 & 0 \\ 0 & 0 & 0 & 0 & 0 & 0 \\ 0 & 0 & 0 & 0 & 0.5 & 0 \\ 0 & 0 & 0 & 0 & 0 & 0 \end{bmatrix} \tag{5.2.1b}$$

where the only component being weighted is the electrical angle.

The control input weight is equal to

$$R = 50. \tag{5.2.1c}$$

And, lastly, the constant weight applied to the instantaneous active power of the system is set as

$$\gamma = 1. \tag{5.2.1d}$$

Note that the running cost matrices no longer incorporate normalizing factors, therefore direct comparisons cannot be made between parameter values. These values were determined heuristically through iteration of weighting parameters.

The simulation output according to these weighting factors is shown below, beginning with the state trajectories in Figure 5.12.

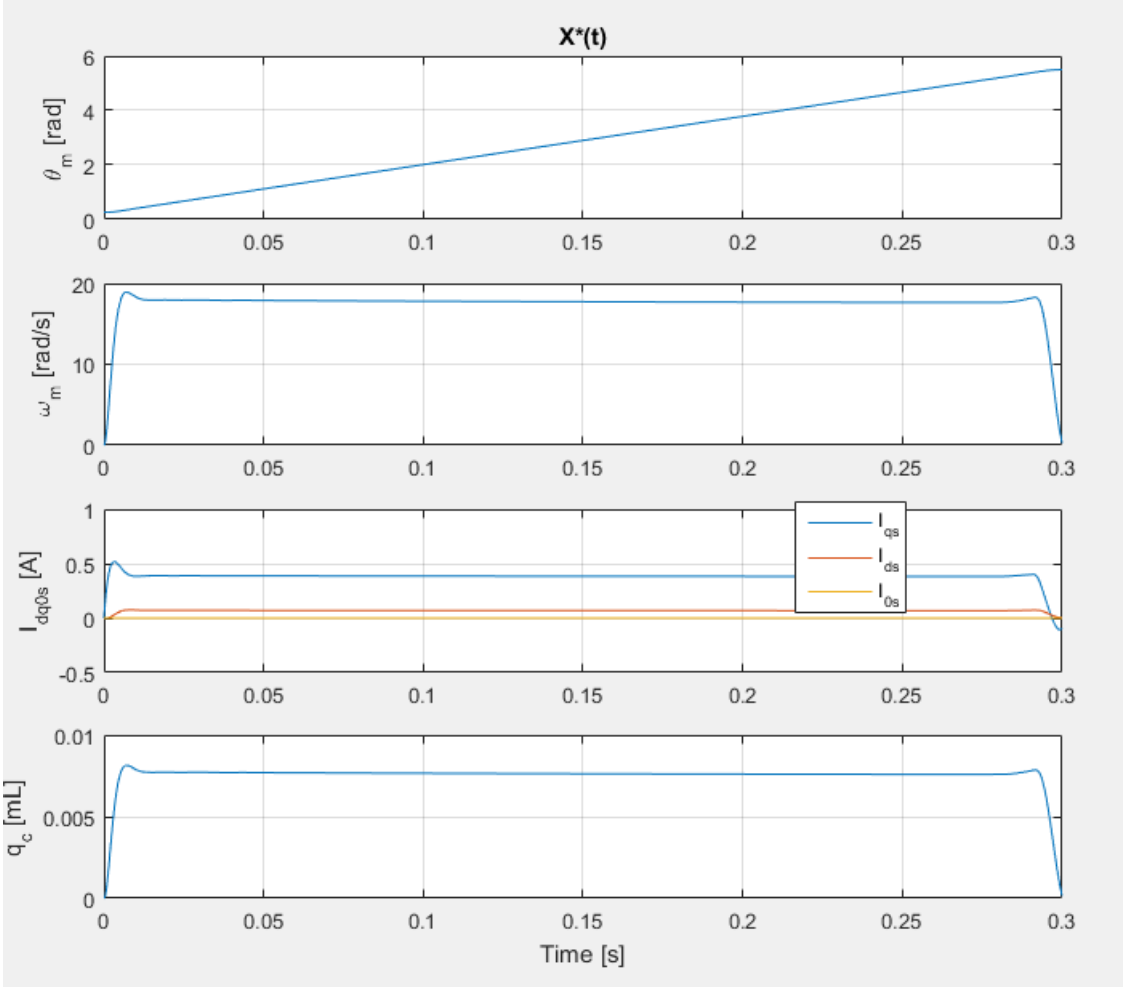

Figure 5.12: Hamiltonian approach optimal state trajectories.

The corresponding control input is shown in Figure 5.13 below.

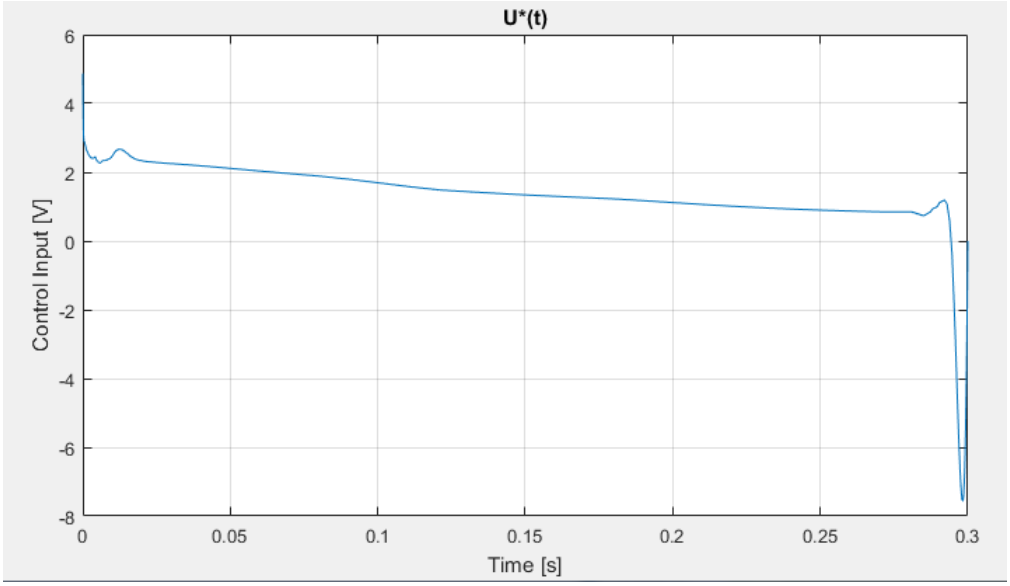

Figure 5.13: Hamiltonian approach optimal control input trajectory.

The nominal angular position output of the Hamiltonian approach follows a very linear trend. Even when the magnitude of the Q matrix term is increased, (which weights the difference between desired and actual position, forcing the system to track to the desired value faster), the overall trend is still linear in appearance.

In order to double check the commanded control input in Figure 5.13, the stroke trajectory was saved and loaded into the PID duty controlled simulation file discussed in Section 5.1.1. Though off by a couple volts in magnitude, the numerically iterated control input has a similar trend to the PID duty controlled solution. The output of the PID simulation is seen in Figure 5.14 below.

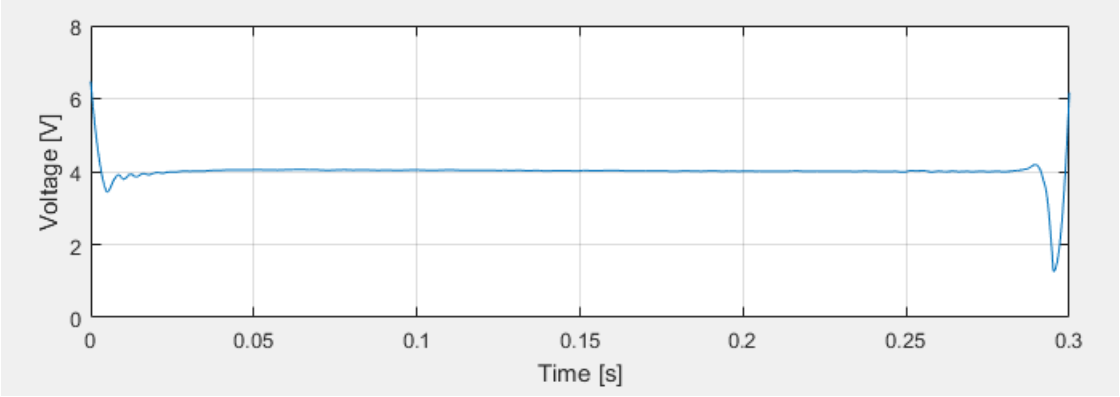

Figure 5.14: Hamiltonian approach control input trajectory after PID simulation.

Running the optimal control solution through the PID simulation is a necessary step in determining required control input because the optimal solver requires linear approximations. These approximations allow the optimal solver to provide a general idea of state and control performance, but they do not show the full nonlinear response. Incorporating the ideal optimal control angular position trajectory into the PID simulation allows for more accurate state and control responses since no approximation is required[2]. See the optimal control simulation flowchart, Figure 8.1, in the Appendix for the full optimal control simulation process.

[2]More instances of optimal control solutions working together with PID control can be seen in references [15, 16, 17].

6. Conclusions

The first goal of this thesis was to create a working, parameterized model for the BLDC motor system operating within the WCS TORVAD^{TM} . Following the work of Krause *et al.*, this was accomplished in both machine variable (ABC) space and rotor-reference variable (dq0) space. Testing at WCS was also performed to characterize motor variable value ranges for parameters such as motor constant and linear damping coefficient. If changes were made to the BLDC motor system, such as scaling the motors for a pediatric TORVAD^{TM}, it would be possible to update the parameters within the simulation to fit new experimental data.

The second goal was to assess the sampling rate effects of the implemented digital PI control on the BLDC motor system. By implementing a PI controlled duty cycle using a zero-order hold method of control effort input, it was determined that the sampling rate used by the engineers at WCS is more than enough for their purposes. By lowering the sampling rate of the micro-controller, it is possible to reduce power consumption of the overall TORVAD^{TM} system while keeping the system controllable and stable, but with the introduction of minor CVS perturbations. Further investigation into the perturbations is required to quantify their severity, therefore it is recommended that the TORVAD^{TM} controller continue operating at its current sampling rate.

The last goal of this thesis was to determine the optimal stroke angle reference trajectory for a single stroke of the BLDC motor system in order to minimize power consumption. This was evaluated through the use of a Linear-Quadratic Tracking method of optimal control and a Hamiltonian approach to optimal control. Both methods utilized a tracking term that drove the system to the desired final position, but only the Hamiltonian approach allowed for explicit weighting of instantaneous active power. Though implemented differently, both optimization techniques produced the same output: a linear approach from starting position to desired position would minimize the average power consumption of the BLDC motor system. From these op-

timization results, a linear reference trajectory is recommended for the power-saving actuation mode of the WCS TORVAD^{TM}.

Though it is recommended purely for power consumption, a linear reference trajectory does not fully emulate the pulsatile nature of the heart. Instead, the trajectory causes the pump to act more like its continuous flow counterparts during actuation[1]. Though this method of actuation saves power, it minimizes one of its most advantageous features: its ability to mimic the pulsatility of the heart by providing in influx of blood flow to the left aorta at an increased pressure than that of a continuous flow pump. This result calls for a more extensive optimal control performance index; one that incorporates both minimization of power consumption and maximization of a new metric that quantifies a measure of pulsatile energy in the flow.

[1]Even with this reference trajectory, the pump would not be running continuously. The pistons would still undergo the transition and momentary 'hold' states between pumping cycles. See Figure 1.1.

7. Future Work

As alluded to earlier, the parameterized model would allow the engineers at WCS to simulate a pediatric BLDC motor system and assess performance before actually constructing one. This saves the company time and money through a simulation guided design process.

Both optimization techniques can be utilized in the future. When used with the linearization about a trajectory form of linearization, the Linear-Quadratic Tracking method has its merits. Since it requires a nominal curve, it can be used to determine if admissible state variations could help better optimize the established trajectory based on adjustable performance criteria. However, if no acceptable nominal trajectory is known, this method becomes much more intensive and must be performed by trial and error with estimated nominal trajectories. The Hamiltonian approach is also useful since it allows for nonlinear cost functional terms, like active power. This method of optimization is preferred due to its ability to provide optimal trajectory information without incorporating bias from nominal trajectory information. The Hamiltonian approach can be especially helpful if more optimal modes of operation are to be incorporated in the future, such as the addition of a pulsatility-based metric as proposed in Chapter 6.

Another consideration would be the use of feedforward coupled with an LQR control scheme. The feedforward would better handle the nonlinearities of the system and the controller would be robust against trajectory change, but a linear approximation of the system would need to be performed at every time iteration within the simulation. This has the potential to be computationally expensive given small time steps or large simulation times since the linearization could not be performed beforehand and used as a reference, as with the LQT method using a known nominal trajectory.

Foreseeable difficulties with incorporating a pulsatility-based metric in the Hamiltonian approach of optimal control include, not only the determination of an accurate

and useful pulsatility-based metric, but also the decision of how to weight this metric in comparison to other considerations such as power consumption minimization. The weighting schemes are typically heuristic in nature, so the weights would need to be decided based on desired performance and design requirements.

8. Appendix

8.1 Nomenclature

Variable	Description	Units
θ_r	Electric angular position of piston	rad
θ_m	Stroke angle of piston	rad
ω_r	Electric angular velocity of piston	$\frac{rad}{s}$
ω_m	Stroke velocity of piston	$\frac{rad}{s}$
λ_{abc}	Magnetic flux of A, B, or C phase of 3-phase power	V*s or Wb

Table 8.1: State variable table.

Parameter	Description	Value	Units
K_P	Proportional Gain of PID controller	600	$\frac{Duty}{rad}$
K_I	Integral Gain of PID controller	800	$\frac{Duty}{rad*s}$
K_D	Derivative Gain of PID controller	8	$\frac{Duty*s}{rad}$

Table 8.2: Section 5 control variable simulation table.

Parameter	Description	Value	Units
R_S	Stator Winding Resistance	2.275	Ohms
L_{ls}	Leakage Inductance in Stator Windings	5.45e-4	H or Ohm*s
L_{ms}	Mutual Inductance in Stator Windings	2.70e-3	H or Ohm*s
P	Stator Poles	10	Poles
$\lambda_m^{'}$	Flux Linkage Amplitude	See Figure 8.2	Wb or A*Ohm*s
B	Linear Damping Coefficient	See Figure 8.4	N*m*s
J_{total}	Moment of Inertia of Piston and Rotor	5.25e-6	kg*m^2

Table 8.3: Section 5 simulation parameter table.

8.2 Optimal Control Simulation Flowchart

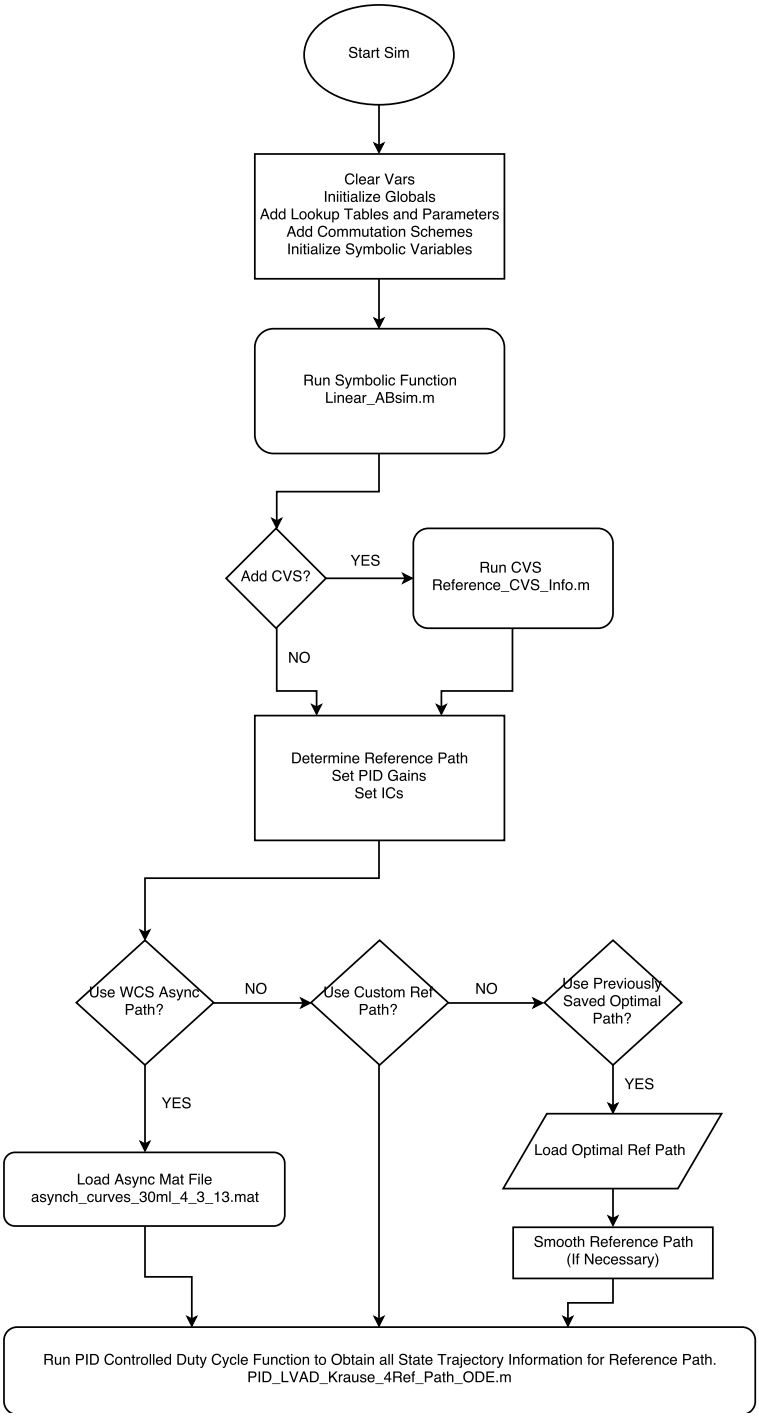

Figure 8.1: Optimal control simulation flowchart.

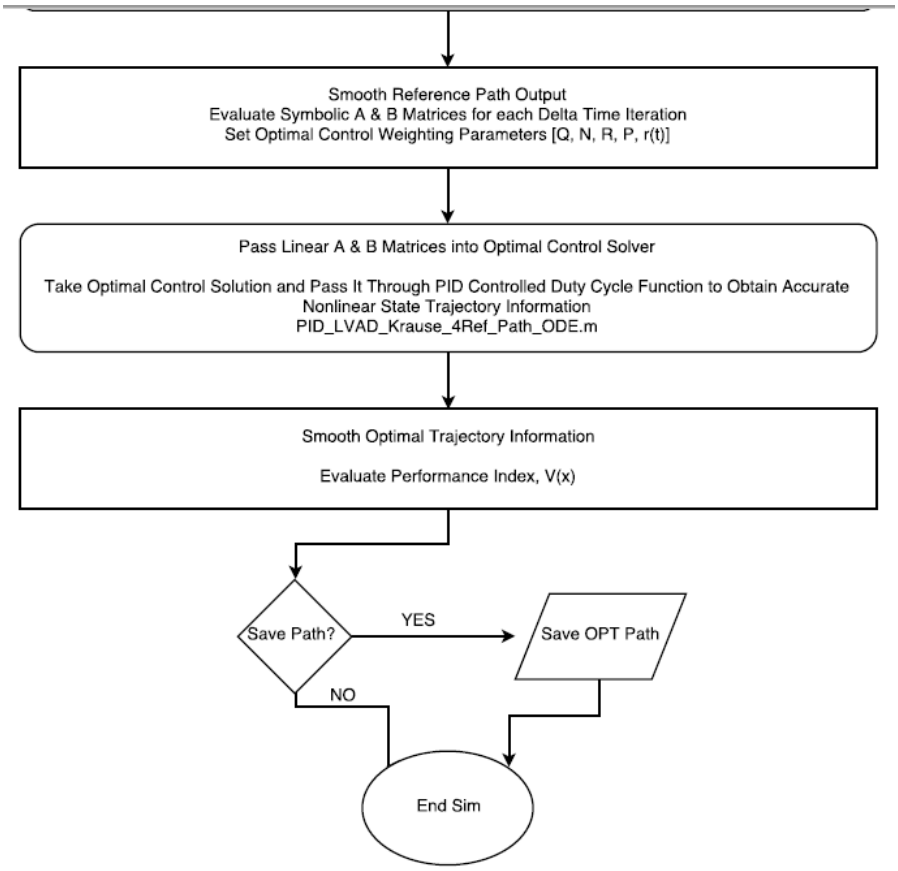

Figure 8.1 cont.

8.3 Experimental Motor Parameter Characterization

Tests using the sinusoidal commutation scheme were performed using the BLDC motors within the TORVAD™ in order to update the unknown parameters in the mathematical models. In the first test, one motor was mounted in place and allowed to spin freely. The maximum motor current amplitudes and average output rotational speed were then documented based on the input duty cycle. This information can be seen below in Table 8.4.

Parameter	Value						
Duty [%]	10	15	20	25	30	40	50
Current [A]	0.0445	0.0555	0.0675	0.0795	0.0905	0.1155	0.1355
Speed [rad/s]	11.38	17.67	23.94	30.2	36.45	48.92	61.61

Table 8.4: Maximum motor current and average rotational speed per duty cycle.

The current and speed results were then used to determine the simulation parameters discussed in Chapter 2 of permanent magnet flux linkage amplitude, $\lambda_m^{'}$, and linear damping coefficient, B, per duty cycle value. Using known parameters, such as moment of inertia, wire resistance and inductance, as well as experimental data, it was possible to iteratively solve for the unknown parameters, $\lambda_m^{'}$ and B, using MATLAB. The iterative process is defined below.

1. Establish potential candidate $\lambda_m^{'}$ and B vectors that include a range of values based around approximations determined through testing. For example, previous tests have been run by WCS determining that the ideal permanent magnet flux linkage amplitude, $\lambda_m^{'}$, for the TORVAD™ motor averaged around 0.1 [V*s/rad] for most duty cycles. Thus, a range of {0.05 – 0.15} [V*s/rad] was used as a vector for the potential values of $\lambda_m^{'}$. Similarly for the damping coefficient, experimental predictions place the value of B around 0.002 [N*m*s/rad], therefore a range of {0 – 0.01} [N*m*s/rad] was used.

2. Choose the desired duty cycle value to apply as control input.

3. Choose a single $\lambda_m^{'}$ and B combination from the candidate vectors and run the ODE solver using the same duty cycle input decided in Part 2.

4. Determine and save error between the simulated output rotational speed and maximum motor current versus the experimental data presented in Table 8.4.
5. Go back to Part 3 until all combinations of $\lambda_m^{'}$ and B have been simulated.
6. Go back to Part 2 until all desired duty cycle values have been simulated.

The results of the iterative process are shown in Table 8.5 below.

Parameter	Values						
Duty [%]	10	15	20	25	30	40	50
$\lambda_m^{'}$ [V*s/rad]	0.1042	0.105	0.1052	0.1054	0.10568	0.1057	0.10586
B [N*m*s/rad]	0.000356	0.00033	0.000324	0.00032	0.000314	0.000315	0.000302

Table 8.5: Simulation parameter results using iterative simulation.

Plotting both parameters versus duty cycle in Microsoft Excel allowed for trendlines, or regression lines, to be determined. The permanent magnet flux linkage amplitude versus duty cycle trend can be seen in Figure 8.2 below.

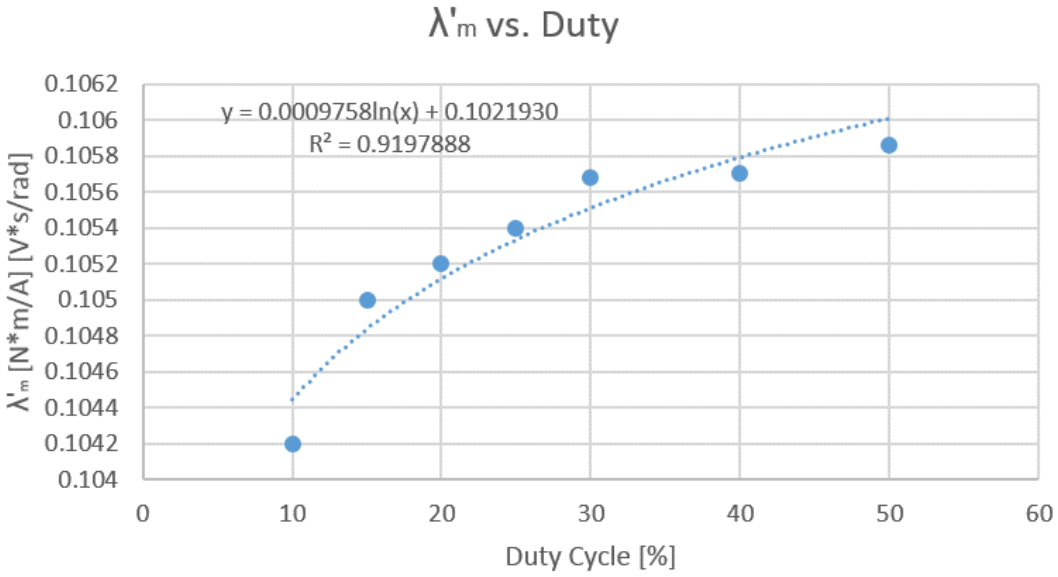

Figure 8.2: Permanent magnet flux linkage versus duty cycle.

Similarly, a trendline was determined for the linear damping coefficient, B, shown in Figure 8.3 below.

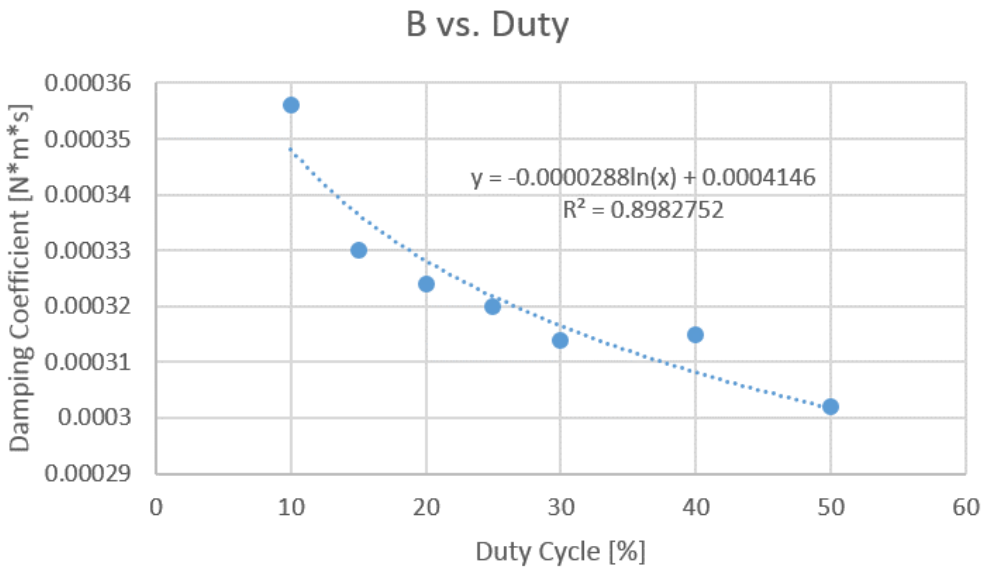

Figure 8.3: Linear damping coefficient versus duty cycle.

A more relevant trend, however, is the linear damping coefficient versus the stroke velocity. This regression line, shown in Figure 8.4, also shows logarithmic decay and has a larger R-squared value.

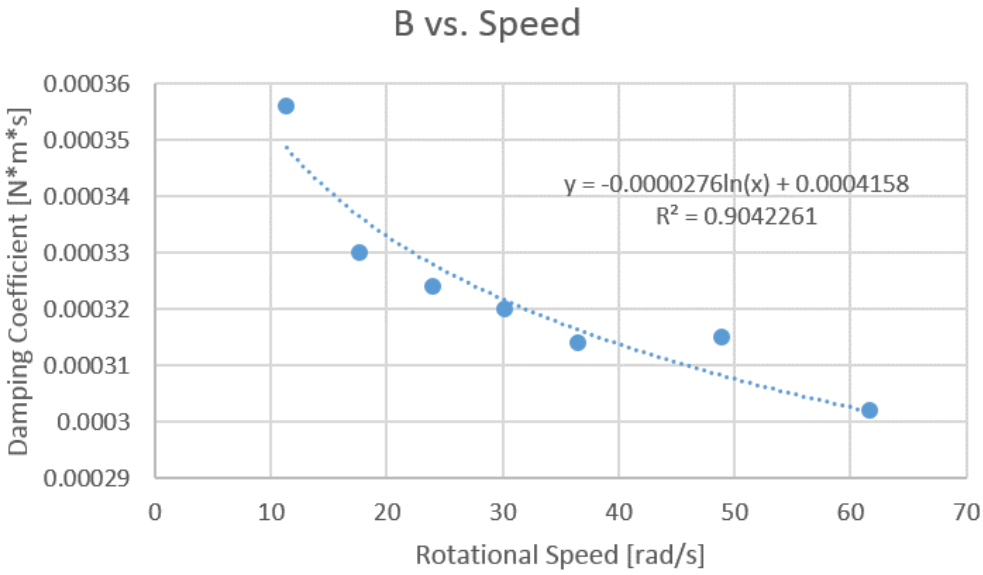

Figure 8.4: Linear damping coefficient versus stroke velocity.

Due to the dynamic changes throughout BLDC motor and optimization simulations, hard coded permanent magnet flux linkage and linear damping coefficient values are not sufficient. Therefore, the logarithmic trendlines in Figures 8.2 and 8.4 are used to update the parameters in every iteration of the simulations[1]. This provides a much more accurate approximation for motor performance when compared to experimental data.

[1]For a negative duty cycle or speed, the trendline equations are evaluated using the absolute value of the duty cycle or stroke velocity, respectively.

9. Bibliography

[1] R. Amacher, J. Asprion, G. Ochsner, H. Tevaearai, M. Wilhelm, A. Plass, A. Amstutz, S. Vandenberghe, and M. Daners, "Numerical Optimal Control of Turbo Dynamic Ventricular Assist Devices," *Bioengineering*, vol. 1, no. 1, pp. 22-46, Dec. 2013.

[2] G.K. Klute, U. Tasch, and D.B. Geselowitz, "An optimal controller for an electric ventricular-assist device: Theory, implementation, and testing," *IEEE Trans. Biomed. Eng.*, pp. 394–403, 1992.

[3] S. Tavoularis, A. Sahrapour, N.U. Ahmed, A. Madrane, and R. Vaillancourt, "Towards optimal control of blood flow in artificial hearts," *Cardiovasc. Eng.*, pp. 2031, 2003.

[4] M. Yoshizawa, H. Takeda, T. Watanabe, M. Miura, T. Yambe, Y. Katahira, and S. Nitta, "An automatic control algorithm for the optimal driving of the ventricular-assist device," *IEEE Trans. Biomed. Eng.*, pp. 243-252, 1992.

[5] P. Krause, O. Wasynczuk, S. Sudhoff, and S. Pekarek, *Analysis of Electric Machinery and Drive Systems*. 3rd ed. Oxford: Clarendon Press, 2013.

[6] R. Crowder, *Electric Drives and Their Controls*. Oxford: Clarendon Press, 1995.

[7] G. Franklin, J. Powell, and A. Emami-Naeini, *Feedback Control of Dynamic Systems*. 5th ed. Prentice Hall, 2006.

[8] Z. Gajic, *Linear Dynamic Systems and Signals*. Prentice Hall, 2003.

[9] D. Liberzon, *Calculus of Variations and Optimal Control Theory.* Princeton: Princeton University Press, 2012.

[10] F. Lewis and V. Syrmos, *Optimal control.* New York: Wiley, 1995.

[11] A. Bryson and Y. Ho, *Applied optimal control.* Washington: Hemisphere Pub. Corp., 1975.

[12] M. E. DeBakey. "The odyssey of the artificial heart." *Artif Organs*, Jun 2000.

[13] A. J. Clegg, D. A. Scott, E. Loveman, J. Colquitt, J. Hutchinson, P. Royle, and J. Bryant, "The clinical and cost-effectiveness of left ventricular assist devices for endstage heart failure: a systematic review and economic evaluation." *Health Technol Assess*, Nov 2005.

[14] Kirklin, D. Naftel, F. Pagani, R. Kormos, L. Stevenson, E. Blume, M. Miller, J. Baldwin and J. Young, "Sixth INTERMACS annual report: A 10,000-patient database", *The Journal of Heart and Lung Transplantation*, vol. 33, no. 6, pp. 555-564, 2014.

[15] G. Yu and R. Hwang, "Optimal PID Speed Control of Brushless DC Motors Using LQR Approach", 2004 *IEEE International Conference on Systems, Man and Cybernetics*, vol. 1, pp. 473-478, 2004.

[16] H. Shieh, Y. Chen and Y. Chiu, "Optimal PID Control System of a Piezoelectric Microospitioner", System Integration, 2008 *IEEE/SICE International Symposium on*, pp. 1-5, 2008.

[17] R. Jan, C. Tseng and R. Liu, "Robust PID control design for permanent magnet synchronous motor: A genetic approach", *Electric Power Systems Research*, vol. 78, no. 7, pp. 1161-1168, 2008.

[18] Gohean, M. George, K. Chang, E. Larson, T. Pate, M. Kurusz, R. Longoria and R. Smalling, "Preservation of Native Aortic Valve Flow and Full Hemodynamic Support with the TORVAD Using a Computational Model of the Cardiovascular System", *ASAIO Journal*, vol. 61, no. 3, pp. 259-265, 2015.

[19] Gohean, M. George, T. Pate, M. Kurusz, R. Longoria and R. Smalling, "Verification of a Computational Cardiovascular System Model Comparing the Hemodynamics of a Continuous Flow to a Synchronous Valveless Pulsatile Flow Left Ventricular Assist Device", *ASAIO Journal*, vol. 59, no. 2, pp. 107-116, 2013.

[20] G. Letsou, T. Pate, J. Gohean, M. Kurusz, R. Longoria, L. Kaiser and R. Smalling, "Improved left ventricular unloading and circulatory support with

synchronized pulsatile left ventricular assistance compared with continuous-flow left ventricular assistance in an acute porcine left ventricular failure model", *The Journal of Thoracic and Cardiovascular Surgery*, vol. 140, no. 5, pp. 1181-1188, 2010.

[21] S. Klotz, A. Jan Danser and D. Burkhoff, "Impact of left ventricular assist device (LVAD) support on the cardiac reverse remodeling process", *Progress in Biophysics and Molecular Biology*, vol. 97, no. 2-3, pp. 479-496, 2008.

[22] D. Nolan, *Sensorless six-step BLDC commutation*, 1st ed. ST, 2016.